

Original Article

Cite this article: Wang Y, Wang X, Zhang S, Chen G, Wu D, Deng H, Tang M, Dang H, and Jian Z. Can ocean heat content regulate Indian summer monsoon rainfall? *Geological Magazine* 161(e4): 1–15. <https://doi.org/10.1017/S0016756824000189>

Received: 28 December 2023

Revised: 23 June 2024

Accepted: 18 July 2024










Keywords:

Upper Ocean heat content; Indian Ocean dipole; Indian summer monsoon rainfall; modern observation; paleoclimate simulation; proxy reconstruction

Corresponding author:

Yue Wang; Email: 163wangyue@tongji.edu.cn

Can ocean heat content regulate Indian summer monsoon rainfall?

Yue Wang^{1,2} , Xingxing Wang¹ , Shuai Zhang³ , Guo Chen² , Daoyu Wu⁴ , Hang Deng² , Minsha Tang² , Haowen Dang¹  and Zhimin Jian¹ 

¹State Key Laboratory of Marine Geology, Tongji University, Shanghai, China; ²School of Ocean and Earth Science, Tongji University, Shanghai, China; ³College of Oceanography, Hohai University, Nanjing, China and ⁴Department of Atmospheric and Oceanic Sciences, Fudan University, Shanghai, China

Abstract

Modern studies suggest that the upper ocean heat content (OHC) in the tropical Indian Ocean (TIO) is a better qualitative predictor of the Indian summer monsoon rainfall (ISMR). But it is still unknown how the OHC is mechanically linked to ISMR and whether it can be applied to long-term climate changes. By analyzing reanalysis datasets across the 20th century, we illustrate that in contrast to those anomalies associated with stronger ISM westerlies, higher ISMR is accompanied with summer surface high pressure and east wind anomalies from the South China Sea to the Bay of Bengal (BOB), and is loosely related to increased western TIO OHC during decayed phases of positive Indian Ocean dipole (IOD) and of El Niño. Except for 1944–1968 AD, this interannually lagged ISMR response to winter OHC is insignificant, probably suppressed by those simultaneous effects of positive IOD and El Niño on ISMR. In our paleoclimatic simulations, this modern observed lagged response is interrupted by seasonally reversed insolation anomalies at the 23,000-year precessional band. Our sensitivity experiments further prove that, the ISMR can be simultaneously reduced by positive IOD-like summer OHC anomalies both for modern and precessional situations. This damping effect is mainly contributed by the warmer western TIO that triggers anomalous surface high pressure, easterly winds, and drastically reduced rainfall from BOB to Arabian Peninsula, but with slightly increased rainfall in the northern ISM region. And the cooler southeastern TIO will only moderately increase rainfall in the southern ISM region.

1. Introduction

The Indian summer monsoon (ISM) exerts significant societal and economic influences on billions of people in Asia. Climatologically, ISM was thought to be induced by seasonal thermal contrast between the Asian continent and the Indian Ocean (IO) (Webster *et al.* 1998; Wang *et al.* 2005; Wu GX *et al.* 2012), but synoptically was argued as a result of the seasonal shift of Intertropical Convergence Zone (Gadgil, 2003, 2018; Geen *et al.* 2020; Yang *et al.* 2023), or a result of moisture or latent heat export from the tropical Indian Ocean (TIO) (Behera *et al.* 1999; Bolton *et al.* 2013; Clemens *et al.* 2021). On seasonal to interannual scales, the forecast skill of ISM largely relies on tropical air–sea coupled climate modes, such as the El Niño–Southern Oscillation (ENSO) and the Indian Ocean Dipole (IOD) (Webster & Yang, 1992; Saji *et al.* 1999; Ashok *et al.* 2001; Fasullo & Webster, 2002; Gadgil *et al.* 2003, 2007; Krishnan *et al.* 2006, 2011; Ashok & Saji, 2007; Wang *et al.* 2013).

For people inhabiting monsoon regions, seasonal variations of the rainfall are more important than wind anomalies. Traditionally, increased ISM rainfall (ISMR) was attributed to La Niña events or positive IOD events (Ashok *et al.* 2004). But modern observed relationships among ENSO, IOD, and ISMR are not stationary and depend on some other factors such as the flavor of ENSO (Kumar *et al.* 1999, 2006; Ashok *et al.* 2007), and the interplay of ENSO and IOD (Ashok *et al.* 2001, 2004; Gadgil *et al.* 2004, 2007; Ashok & Saji, 2007; Ihara *et al.* 2007; Li *et al.* 2016). Due to the concurrence of La Niña and negative IOD (or El Niño and positive IOD), the effect of IOD on ISMR tends to cancel that of ENSO (depending on the phases and strengths of two modes) (Ashok *et al.* 2001; Gadgil *et al.* 2004). Thus, ENSO itself explains only 30% of the interannual variability of ISMR in observations (Gadgil, 2014), and atmospheric general circulation models (AGCMs) with ENSO-related sea surface temperature (SST) as boundary conditions have poor skill of simulation of ISMR variations (Gadgil *et al.* 2007; Gadgil & Srinivasan, 2011). This indicates the tenuousness of relying on ENSO for ISMR predictions (Pottapinjala *et al.* 2016). Fortunately, Krishnan *et al.* (2011) found that if AGCMs were coupled to a slab-ocean model with varied mixed-layer depth in TIO, then the model could correctly simulate the observed ISMR changes during positive IOD events. It means that we can further improve the forecast skill of ISMR by considering air–sea coupling (Kumar *et al.* 2005), or

© The Author(s), 2024. Published by Cambridge University Press. This is an Open Access article, distributed under the terms of the Creative Commons Attribution licence (<https://creativecommons.org/licenses/by/4.0/>), which permits unrestricted re-use, distribution and reproduction, provided the original article is properly cited.



directly accounting for oceanic moisture and latent heat supplement of ISMR in the TIO (Behera *et al.* 1999; Krishnan *et al.* 2006).

From an energetic viewpoint, the ocean is the largest heat capacitor of the earth's climate system and a main source of atmospheric moist static energy (MSE). While the summer monsoon transports huge water vapor and latent heat from tropical oceans into continents (Trenberth *et al.* 2000; Fasullo & Trenberth, 2008; Trenberth & Fasullo, 2013; Wang *et al.* 2014, 2017; Biasutti *et al.* 2018), it has been proved to be greatly modulated by heat storage or transport anomalies in tropical oceans across different time scales (Jalihal *et al.* 2019a, 2019b; Lutsko *et al.* 2019; Yang YP *et al.* 2019). Since the ocean thermal energy required for fueling monsoon circulations comes from the upper ocean rather than the sea surface, upper ocean heat content (OHC) changes in the tropics can be taken as the heat engine of global monsoon (Cheng *et al.* 2017, 2022; Hill, 2019; Jian *et al.* 2022).

At modern seasonal or interannual scales, upper OHC anomalies associated with ENSO or ENSO-like conditions in the tropical Pacific or Atlantic oceans have been proposed as precursors of ISMR (Rajeevan & McPhaden, 2004; Rajeevan & Pai, 2007; Pottapinjala *et al.* 2016). But recent observations suggest that (Ali *et al.* 2015; Venugopal *et al.* 2018), at least from the year 1993 to 2017 AD, the mixed layer OHC or mean temperature above 26°C in the southwest TIO during boreal winter–spring is a better qualitative predictor of ISMR than those Pacific ENSO indexes. This may be explained by the Indo-Pacific Ocean Capacitor effect (IPOC) (Xie *et al.* 2002, 2009, 2016; Du *et al.* 2009, 2011): El Niño events can induce anomalous atmospheric downward motions and easterlies in the eastern TIO (EIO), and associated ocean wave dynamics will increase the upper OHC in the western TIO (WIO) during the following winter. After multiple air–sea coupled feedbacks, warmer SST emerges in the northern IO (NIO) and anomalous atmospheric anticyclonic circulation (AAC) extends from the Northwest Pacific to the Bay of Bengal (BOB) during boreal summer. While the surface easterlies south of the AAC greatly suppress the ISM westerlies, the warmer NIO was argued to have provided more evaporated moisture for the increased ISM rainfall over western and southern India (Mishra *et al.* 2012; Xie *et al.* 2016; Darshana *et al.* 2020).

It should be noted that IPOC-associated winter OHC anomalies may be also triggered by positive IOD events (Chen *et al.* 2021; Du *et al.* 2022, 2023). And the summer OHC seesaw along the equatorial IO (with warmer WIO and cooler EIO) itself is a robust index of IOD development (McPhaden & Nagura 2013). Although many studies have emphasized the role of a cooler EIO on the increased ISMR from intraseasonal to interannual time scales (Ashok *et al.* 2004; Krishnan *et al.* 2006, 2011), the long-term relationships among IOD, TIO OHC, and ISMR are still unclear either in historical periods or in geological periods.

In this study, we first distinguished those air–sea coupled changes related to ISMR from those related to ISM wind and highlighted the role of IOD-associated OHC (especially in WIO) on ISMR by analyzing reanalysis datasets across the 20th century. Then from a paleoclimatic perspective, we explored the relations of TIO OHC anomalies and ISMR at the 23,000 years' precessional time scales, based on simulations of air–sea coupled model (and its atmospheric component) under orbital insolation and GHG forcings. Despite different time scales and external forcings, both modern observation and paleoclimate simulation suggest a significant modulation of summer positive IOD-like OHC pattern on ISMR.

2. Data, models, and methods

2.a. Modern observations

Atmospheric variables (such as surface pressure, 850 hPa wind fields, rainfall) come from the monthly mean NOAA-CIRES-DOE 20th Century Reanalysis version 3 (20CRv3) of 1° resolution spanning from the year 1836 to 2015 AD (Slivinski *et al.* 2019, 2021) (https://psl.noaa.gov/data/gridded/data.20thC_ReanV3.html). Ocean temperature used for calculating OHC comes from the monthly mean Simple Ocean Data Assimilation (SODA) reanalysis dataset (version 2.2.4) with 0.5° horizontal resolution and vertical 40 layers spanning from the year 1871 to 2010 AD (Carton *et al.* 2012) (https://apdrc.soest.hawaii.edu/datadoc/soda_2.2.4.php). The upper OHC above 26°C (OHC26, Joules m⁻²) is calculated according to the following equation (Pu *et al.* 2003; Yang XX *et al.* 2019):

$$OHC = \int_z^0 C_p * \rho * T * dz = C_p * \sum_{i=1}^n (\rho_i * T_i * dZ_i)$$

Here, C_p is the heat capacity of sea water taken as 4178 J kg⁻¹ °C⁻¹, ρ is potential density, T is ocean temperature, z is the depth of 26°C isotherm, n is the total layers from surface to the depth z , and ρ_i , T_i , dZ_i are density, temperature, and layer thickness for the layer i . The regional averaged January–February–March (JFM) OHC26 over the western Indian Ocean (WIO, 5° S–15° N, 40° E–60° E) is named as OHC26_{WIO}.

According to Li & Zeng (2002), the ISM wind intensity is defined as June–July–August–September (JJAS) averaged Dynamical Normalized Seasonality (DNS) index of 850 hPa winds within the South Asian domain (5° N–22.5° N, 35° E–97.5° E), calculated using the 20CRv3 reanalysis dataset. The ISMR is defined as the area-weighted average of the JJAS rainfall of all the 36 meteorological subdivisions in India during the time period 1871–2016 (Kothawale *et al.* 2017) (downloaded from https://tropmet.res.in/static_pages.php?page_id=53). For the intensity of IOD and ENSO, we use the Dipole Mode Index (DMI) (Saji *et al.* 1999) and the Southern Oscillation Index (SOI) (Ropelewski & Jones, 1987) from NOAA Physical Sciences Laboratory (PSL) website (https://psl.noaa.gov/gcos_wgsp/Timeseries). Here, DMI was calculated as August–September–October (ASO) mean time series and to resolve the seasonal evolution of ENSO–ISM relationship (Wu RG *et al.* 2012; Chakraborty, 2018), SOI was calculated as June–July–August (JJA) mean and December–January–February (DJF) mean time series (called SOI_{JJA} and SOI_{DJF}), respectively.

In Figure 1, the lead-lag cross correlation (R) of two time series was calculated using the Past software (version 4.03) (Hammer *et al.* 2001). Given that ISMR and OHC26 are both influenced by multiple parameters, we do not expect there to be an extremely good correlation between a single parameter and ISMR (or OHC26_{WIO}). We also do not attempt to quantitatively predict ISMR using other parameters, but only qualitatively illustrate the linkage among ENSO, IOD, OHC, and ISMR at interannual time scale. Considering that this relationship may be not stationary, the 20-year moving correlation of two time series was calculated using the Matlab program written by David De Vleeschouwer (De Vleeschouwer, 2010). In Figures 2 and 3, linear regression analysis was conducted for different variables (such as surface pressure, 850 hPa wind fields, rainfall, OHC26) against the normalized time series of a specific index (i.e., DNS, ISMR, SOI, DMI, and OHC26_{WIO}), using the NCAR Command Language

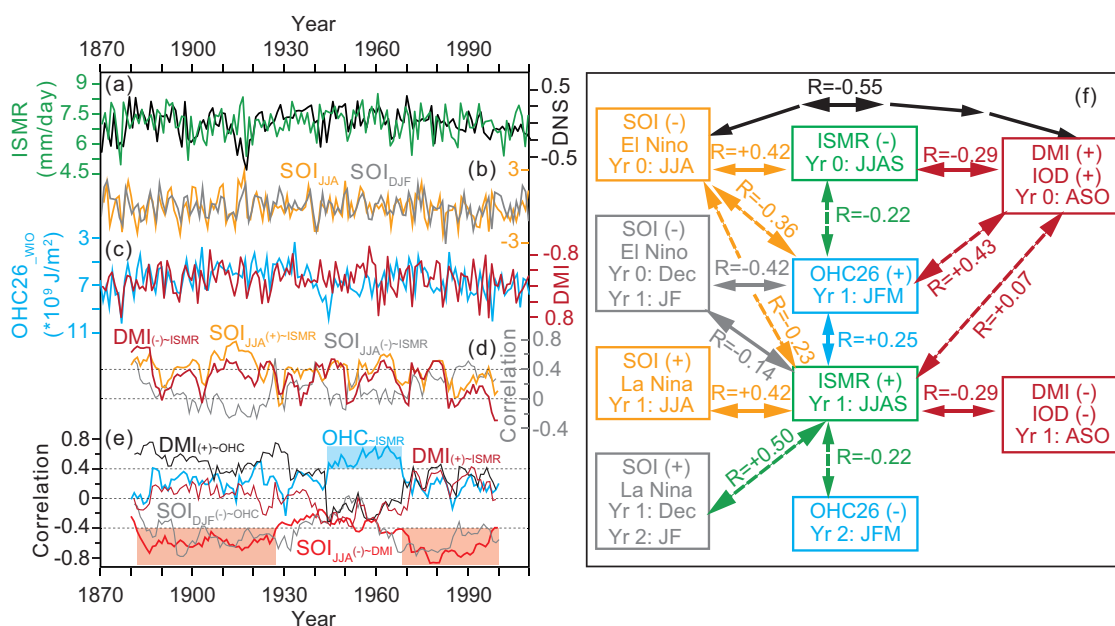


Figure 1. (Colour online) (a) Modern observed time series of ISMR rainfall index (ISMR, green line) and ISM wind index (DNS, with linear trend removed, no units) from the year 1871 to 2010 AD. (b) Time series of SOI indexes during DJF and JJA (gray line for SOI_{DJF} and orange line for SOI_{JJA} , no units). (c) ASO DMI index (brown line, units: K) is compared with the OHC26_WIO time series (cyan line). (d) 20-year moving correlations for ISMR in Yr 1 with three indexes: DMI(-) in Yr 1 (multiplied by -1, brown line), $SOI_{JJA}(+)$ in Yr 1 (orange line), $SOI_{JJA}(-)$ in Yr 0 (gray line). (e) Moving correlations for OHC26_WIO in Yr 1 with three indexes: ISMR(+) in Yr 1 (cyan line), DMI(+) in Yr 0 (black line), $SOI_{DJF}(-)$ in Yr 1 (gray line), and for DMI(+) in Yr 0 with two indexes: ISMR(+) in Yr 1 (brown line), $SOI_{JJA}(-)$ in Yr 0 (red line). (f) Lead-lag correlations (R) between different time series. In (d), (e), and (f), those positive or negative signs in parentheses show the anomalous status of SOI, DMI, OHC26, and ISMR in the corresponding year.

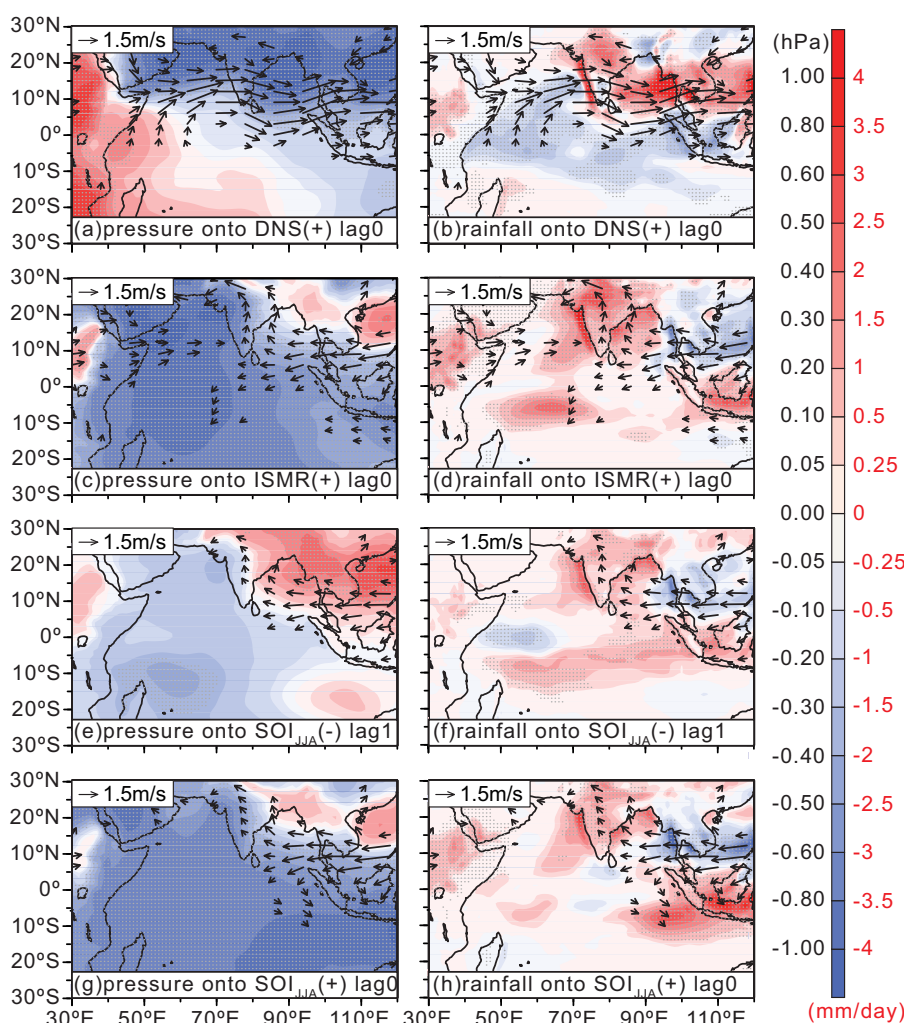


Figure 2. (Colour online) (a) Regression coefficients of JJAS surface pressure (shaded) and 850 hPa horizontal winds (vector) against the normalized time series of ISM wind index (DNS). (b) is the same as (a) but with surface pressure replaced by JJAS rainfall (shaded). (c)–(d), (e)–(f), (g)–(h) are the same as (a)–(b) but for regression coefficients against the normalized time series of ISMR, of $SOI_{JJA}*(-1)$ in 1 year before, and of SOI_{JJA} in the same year, respectively. Unless otherwise stated, grey dotted areas in all regression figures are significant at the 95% level with Student's *t*-test, and small wind vectors (magnitude < 0.5 m/s) are not shown for clarity. For regression results, the character “(+)” or “(-)” means the normalized time series was multiplied by +1 or -1, and the character “lag0” or “lag1” means dependent variable lags independent variable (or the normalized time series) by 0 or 1 year.

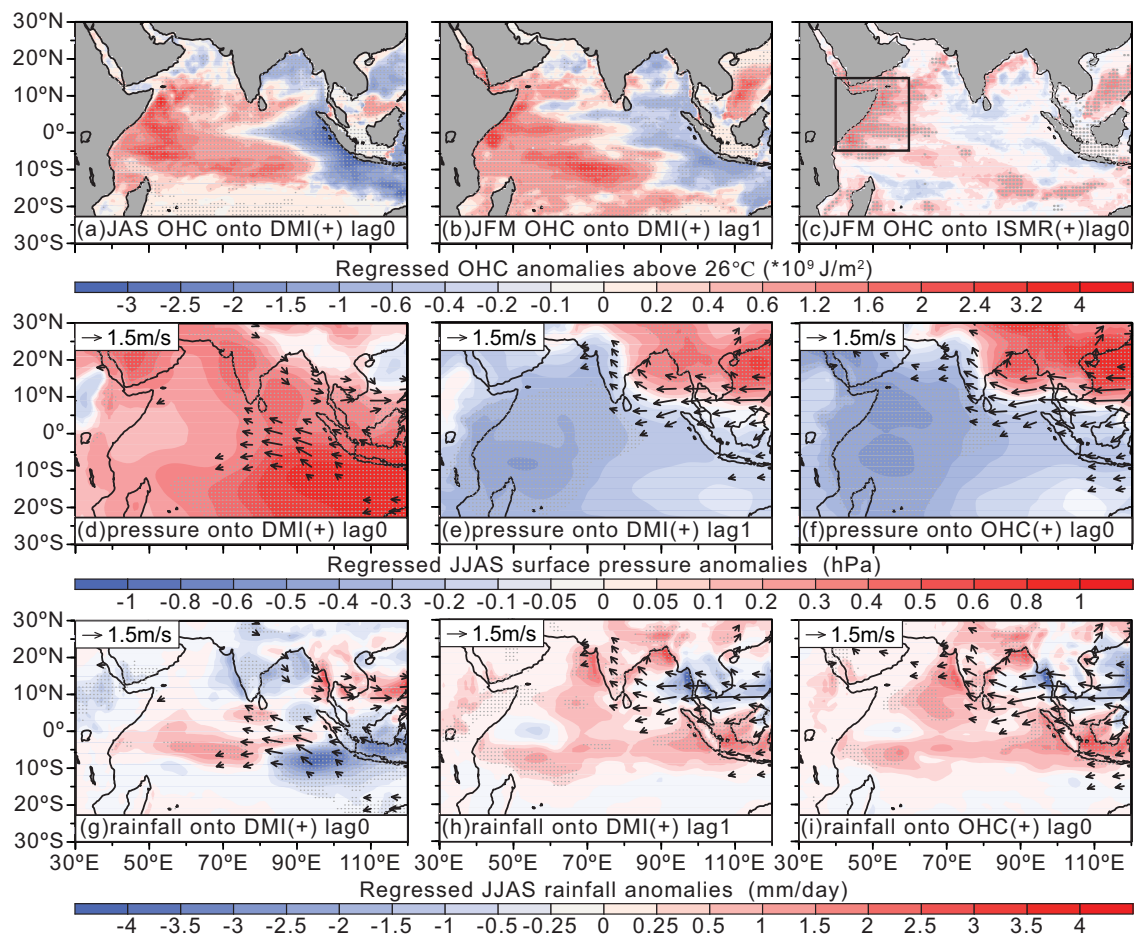


Figure 3. (Colour online) Regression coefficients against modern observed time series (normalized). (a)–(b) are JAS and JFM OHC against the normalized DMI time series. (c) JFM OHC against ISMR time series. (d)–(e) JJAS surface pressure (shaded) and 850 hPa horizontal winds (vector) against DMI time series. (f) JJAS surface pressure (shaded) and 850 hPa horizontal winds (vector) against the OHC26_{WIO} time series. (g)–(i) are the same as (d)–(f) but with surface pressure replaced by JJAS rainfall (shaded). Black rectangular in (c) represents the region of WIO (5° S–15° N, 40° E–60° E) for calculating the OHC26_{WIO} time series. Note that the character of “lag0” in (c), (f) and (i) is relative to the year of higher ISMR or OHC26_{WIO} (Yr 1), and in other panels is relative to the year of higher DMI (Yr 0).

(version 6.6.2). Monthly mean SST in TIO were also regressed onto the normalized DMI index for further sensitivity experiments (see section 2.c), and their JFM and July–August–September (JAS) means are shown in Figure 4.

2.b. Paleoclimate simulations and proxies

As in Jian *et al.* (2022), here we used the outputs from transient accelerated simulations of the Community Earth System Model 1.0.4 (CESM) (Shields *et al.* 2012), and of the water isotope ($\delta^{18}\text{O}$)-enabled air–sea coupled climate model from Goddard Institute for Space Studies of USA (GISS_ModelE2-R model) (Lewis *et al.* 2014; Schmidt *et al.* 2014). The CESM was configured with T31_gx3v7 resolution ($3.75^\circ \times 3.75^\circ$ and vertical 27 levels for atmosphere, nominal 3° resolution, and vertical 60 levels for ocean). The GISS_ModelE2-R model has a horizontal resolution of 4° latitude $\times 5^\circ$ longitude (both for the atmosphere and ocean), with 20 vertical layers in the atmosphere (up to 0.1 hPa) and 13 vertical layers in the Russell Ocean model (Russell *et al.* 1995, 2000). Water isotope tracers ($^1\text{H}_2$ ^{16}O , “normal” water; ^2H ^1H ^{16}O or HDO, reported as δD ; and $^1\text{H}_2$ ^{18}O , $\delta^{18}\text{O}$) are incorporated into the atmosphere, land surface, sea ice, and ocean (Schmidt *et al.* 2005).

As a spin-up, these two models were run for 200 model years under fixed orbital parameters and greenhouse gases (GHG) of 300 ka BP, with all other boundary conditions (but neglecting ice sheet changes) set for their values in 1950 AD. Then, the models were integrated for 3000 model years with the transient orbital insolation forcing and GHG forcing of the last 300,000 years, in which orbital parameters and GHG were both advanced by 100 years at the end of each model year (Kutzbach *et al.* 2008). These two transient experiments are called CESM_ghg and GISS_ghg, respectively, and their outputs for the last 3000 model years are used in our analysis.

For experiment CESM_ghg, OHC above 26°C was first calculated using the same method as in modern observation, and then was linearly regressed onto the normalized ISMR index (Figs. 5a–c). Similar regression analysis was also applied to atmospheric variables (rainfall, horizontal winds and vertical p velocity) (Figs. 5d–f). Regionally averaged time series are calculated for annual mean SST over the Western Indian Ocean (10°S – 10°N , 50°E – 70°E , named as WIO_SST_{CESM}) and Eastern Indian Ocean (10°S – 0°N , 85°E – 105°E , called EIO_SST_{CESM}) to further calculate Dipole Mode Index (called DMI_{CESM}) (Figs. 6b–d, as in Wang *et al.* 2015). Note that regional averaged time series of WIO, EIO, and DMI based on OHC26 are nearly the same as those of

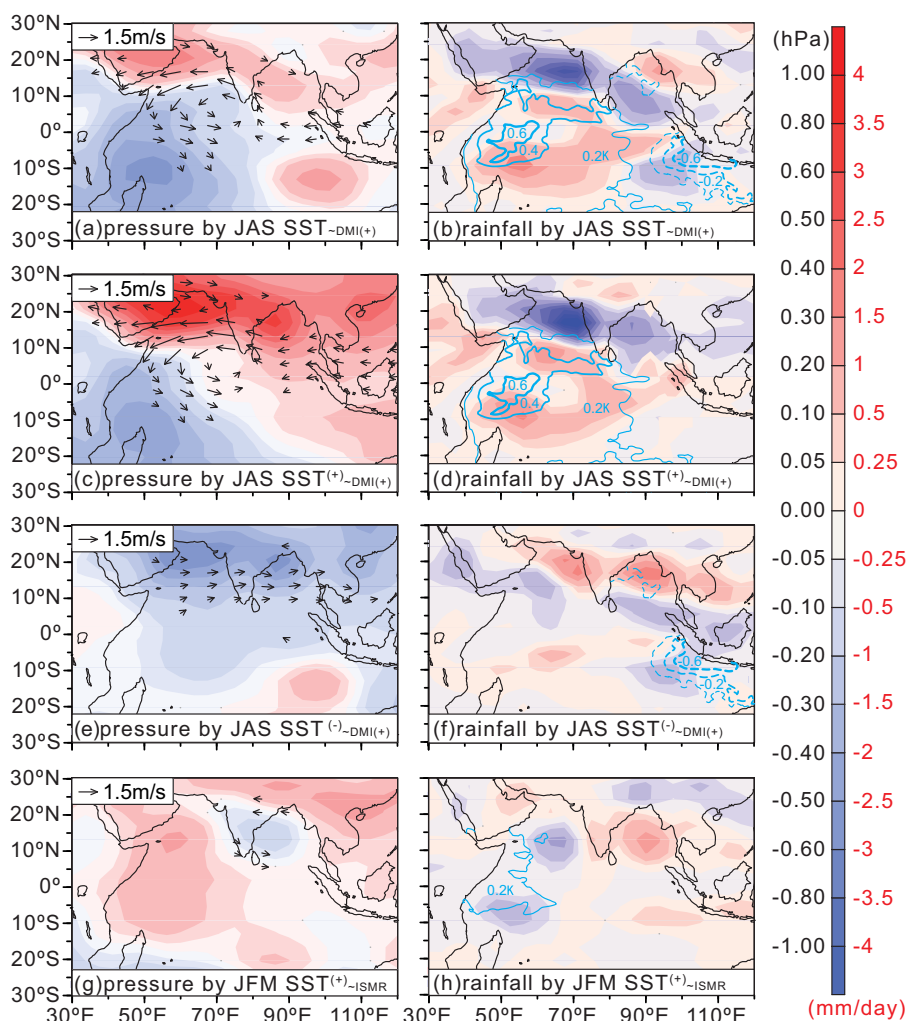


Figure 4. (Colour online) Composite differences of JJAS atmospheric variables between experiments CAM_control-TIOsst_JAS and CAM_control (a–b), between experiments CAM_control-TIOsst_JASP and CAM_control (c–d), between experiments CAM_control-TIOsst_JASN and CAM_control (e–f), and between experiments CAM_control-WIOsst_jfmP and CAM_control (g–h). The left panels are surface pressure (shaded) and 850 hPa winds (vectors, small winds (magnitude < 0.5 m/s) are not shown). The right panels are the same as the left panels but with surface pressure replaced by rainfall (shaded). Cyan contours and numbers in (b), (d), (f), and (h) show the spatial distributions of SST anomalies prescribed in each experiment. Characters of “~DMI(+)” or “~ISMIR” means that these SST anomalies are regressed onto the DMI or ISMR maximum.

ocean mean temperature above 26°C and of SST, only time series of SST are shown in Fig. 6 for better comparison with paleo-proxy. ISMR_CESM and ISMR_GISS (Fig. 6e) represent regional averaged JJAS land rainfall from experiments CESM_ghg and GISS_ghg over the Indian subcontinent (10° N–30° N, 70° E–90° E), respectively. As referred to as $\delta^{18}\text{O}_{\text{sw_GISS}}$ (Fig. 6f), the annual mean $\delta^{18}\text{O}$ of sea surface water ($\delta^{18}\text{O}_{\text{sw}}$) from experiment GISS_ghg is regionally averaged over the Bay of Bengal (7° N–22° N, 80° E–100° E).

Paleo-proxies used in Figure 6 are summarized in Table 1, including the planktonic foraminifera *Globigerinoides ruber* Mg/Ca-SST record of core WIND28K from the SWIO, the alkenone temperature ($U^K_{37}\text{-SST}$) stacks of five cores from the WIO (GeoB3005, TY93929, MD85668, MD85674, VM19-193), and of three cores from the EIO (GeoB10038, SO139-74KL, MD2152). $U^K_{37}\text{-SST}$ based DMI was the difference between WIO and EIO. As a proxy of ISMR, ice-volume corrected $\delta^{18}\text{O}_{\text{sw}}$ was stacked by two cores from the Bay of Bengal (SO188-17286, U1446). All time series of paleo-proxy are interpolated to 1ka interval.

2.c. Equilibrium experiments with prescribed SST anomalies

Note that our transient simulations of CESM_ghg and GISS_ghg are both forced by atmospheric CO_2 changes of 100 ppmv and seasonal solar insolation changes of about 80 W/m^2 . These two

experiments enable us to investigate more acute changes of ISMR and its linkage with upper ocean thermal anomalies under extreme geological boundary conditions. Especially, the precessional insolation changes are much larger than those insolation changes at 41,000 years’ obliquity (about 30 W/m^2) and the radiative forcing of CO_2 doubling (3.7 W/m^2). Thus, to compare with modern interannual variabilities without external forcing, here, we only focus on those paleoclimate changes at precessional band but neglect the effect of obliquity and CO_2 .

To isolate the role of IOD-like SST anomalies on ISMR, we also used outputs from equilibrium experiments of the CESM and its atmospheric component (the Community Atmospheric Model version 4, CAM4). Here, the CESM/CAM4 was run for 200/100 model years for each experiment, and the model outputs of the last 100/30 model years are analyzed. As detailed in Wang *et al.* (2016), the experiments CESM_control, CESM_P_min, CAM_control, and CAM_P_min are all set up with modern (1950_AD) greenhouse gas concentrations, topography, and land–sea distributions. The only difference between “control” and “P_min” is precessional parameter (0.0169 vs –0.0169), and here “P_min” actually means a precessional minimum of winter insolation and a maximum of summer insolation, respectively. Note that experiments CESM_P_min and CESM_control will dynamically calculate SST (as a result of air–sea interactions) and their differences are treated as precession forced SST anomalies. To exclude the impact of these SST anomalies,

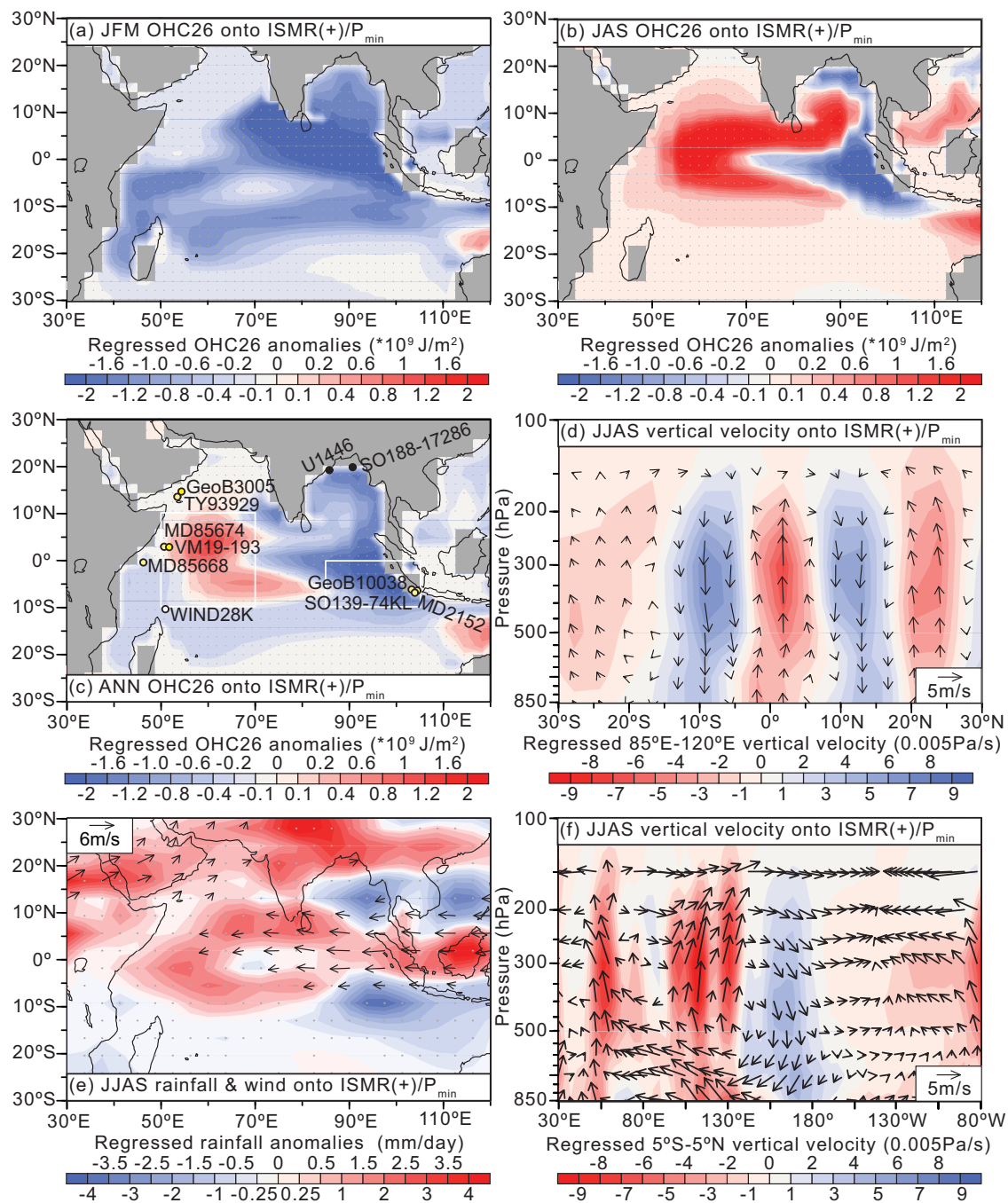


Figure 5. (Colour online) Regression coefficients against the normalized time series of $ISMR_{CESM}$ from experiment $CESM_{ghg}$. (a)–(c) are JFM, JAS and annual mean OHC. (d) JJAS vertical p velocity (shaded) and meridional vertical circulation (vectors; meridional wind v and vertical p velocity) along the longitudes 85° E– 120° E, (e) JJAS rainfall (shaded) and 850 hPa horizontal winds (vectors, small winds (magnitude < 2 m/s) are not shown). (f) JJAS vertical p velocity (shaded) and zonal-vertical circulation (vectors; zonal wind u and vertical p velocity) along the latitudes 5° S– 5° N. White rectangular in (c) show the WIO and EIO regions for calculating DMI in simulations (Wang et al. 2015). Yellow, white, and black filled dots in (c) show site locations of paleo-proxies (U^{K}_{37} -SST, Mg/Ca-SST and $\delta^{18}O_{sw}$). Character “ISMR(+)/ P_{min} ” means that these anomalies are regressed onto the ISMR maximum (also the minimum of precession parameter).

experiments $CAM_{control}$ and $CAM_{P_{min}}$ are prescribed with the same modern climatological monthly mean SST.

The equilibrium experiment $CAM_{P_{min-nptsst}}$ is the same as $CAM_{P_{min}}$ but with modified SST over the North Pacific (20° N– 50° N, 120° E– 120° W) and tropical Pacific (20° S– 20° N, 110° E– 80° W). In these regions, precession forced climatological monthly mean SST anomalies are added to their modern values. Similarly, SST anomalies over TIO (20° S– 25° N, 40° E– 109° E) are

added to $CAM_{P_{min}}$ in four different ways: (1) using values of 12 months (experiment $CAM_{P_{min-TIOsst}}$), (2) only using values during JJA (experiment $CAM_{P_{min-TIOsst-JJA}}$), (3) only using positive values during JJA (experiment $CAM_{P_{min-TIOsst-JJAP}}$), and (4) only using negative values during JJA (experiment $CAM_{P_{min-TIOsst-JJAN}}$).

As a comparison, by regressing onto the modern observed DMI index, monthly TIO SST anomalies during July–August–

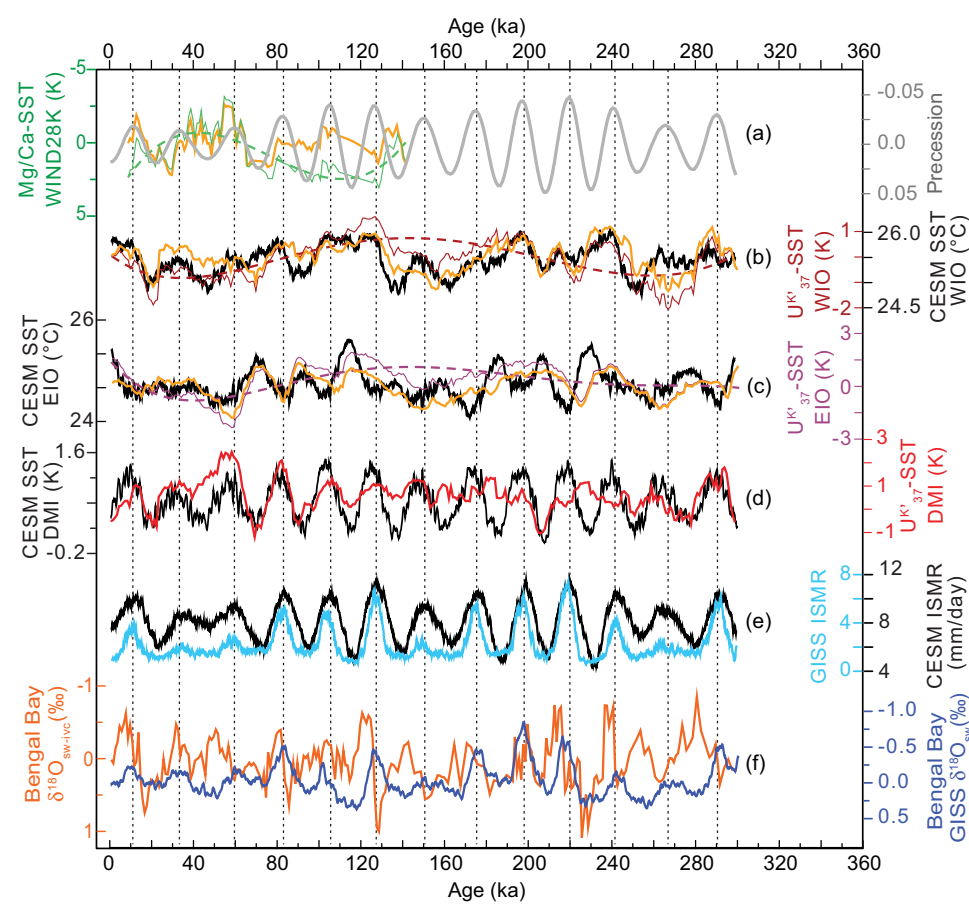


Figure 6. (Colour online) Regional averaged time series of WIO_SST_CESM, EIO_SST_CESM, DMI_CESM, ISMR_CESM, ISMR_GISS, and $\delta^{18}\text{O}_{\text{sw-GISS}}$ from experiments CESM_ghg (black lines) and GISS_ghg (cyan and blue lines) are compared with multiple paleo-proxies: (a) Mg/Ca-SST of core WIND28K from the southwest Indian Ocean, (b) WIO stacked $U^{K'}_{37}$ -SST, (c) EIO stacked $U^{K'}_{37}$ -SST, (d) $U^{K'}_{37}$ -SST based DMI, (f) the Bengal Bay $\delta^{18}\text{O}_{\text{sw-ivc}}$. In (a)–(c), orange solid lines are residuals by subtracting 5-order polynomial-fitted trends (dashed lines) from the original time series (thin solid lines). The gray thick line in (a) is the precession parameter (Laskar *et al.* 2004), and its minimas are marked by black vertical dashed lines.

Table 1. Paleo-proxy information used in this study

Core name	Longitude (°E)	Latitude (°N)	Water depth (m)	Record length (ka)	Proxy (reference)
SO188-17286	90.88	19.74	1428	0–130	$\delta^{18}\text{O}_{\text{sw}}$ (Lauterbach <i>et al.</i> 2020)
U1446	85.73	19.08	1430	0–1500	$\delta^{18}\text{O}_{\text{sw}}$ (Clemens <i>et al.</i> 2021)
GeoB10038	103.25	−5.90	1819	0–132	$U^{K'}_{37}$ -SST (Mohtadi <i>et al.</i> 2010a, 2010b)
SO139-74KL	103.83	−6.54	1690	1–292	$U^{K'}_{37}$ -SST (Lückge <i>et al.</i> 2009)
MD98-2152	103.88	−6.38	1796	0–450	$U^{K'}_{37}$ -SST (Windler <i>et al.</i> 2019)
TY93929/P (NIOP929)	53.25	13.70	2490	2–153 (94–153)	$U^{K'}_{37}$ -SST (Bard <i>et al.</i> 1997; Rostek <i>et al.</i> 1997; Saher <i>et al.</i> 2007, 2009)
MD85674	50.43	3.183	4875	0–149	$U^{K'}_{37}$ -SST (Bard <i>et al.</i> 1997)
MD85668	46.03	0.00	4020	0–152	$U^{K'}_{37}$ -SST (Bard <i>et al.</i> 1997)
GeoB3005	54.37	14.97	2314	0–307	$U^{K'}_{37}$ -SST (Budziak <i>et al.</i> 2000)
VM19-193	51.47	2.98	5106	7–248	$U^{K'}_{37}$ -SST (Windler <i>et al.</i> 2023)
WIND28K	51.00	−10.20	4157	8–142	Mg/Ca-SST (Kiefer <i>et al.</i> 2006; Johnstone <i>et al.</i> 2014)

September (JAS) are added to experiment CAM_{control} in similar ways, resulting in another three equilibrium experiments: CAM_{control-TIOsst_JAS}, CAM_{control-TIOsst_JASp}, and CAM_{control-TIOsst_JASn}. Although summer NIO warming has been argued as a bridge from winter OHC to ISMR (Darshana *et al.* 2020), this mechanism should be better tested by the “pacemaker experiment” of fully coupled CESM model (Zhang *et al.* 2019), which has

beyond our ability. Thus, in experiment CAM_{control-WIOsst_jfmP}, we only use the JFM SST warming anomalies in WIO (5° S–15° N, 40° E–60° E) that are significantly correlated with modern observed ISMR index. It should be noted that these CAM4 experiments can only assess the direct impact of TIO SST on ISMR through atmospheric processes, but left the indirect influence through air–sea coupled feedbacks to future studies.

3. Results and discussion

3.a. Distinct modern dynamics associated with ISM wind and rainfall

Based on historical observations from the year 1871 to 2010 AD, we first compare the ISMR and the detrended DNS time series (Fig. 1a). Since the DNS is highly correlated with the South Asian (5°N – 22.5°N , 35°E – 97.5°E) averaged zonal wind at 850 hPa ($R = +0.86$, $\text{lag}=0$, $p = 1.18 \times 10^{-42}$), it is a reliable ISM wind intensity index. The correlation between DNS and ISMR is only $+0.26$ ($\text{lag} = 0$, $p = 0.002$), largely due to their similarity on multidecadal time scales. By comparing regression coefficients against the DNS index and the ISMR index, we found that they are associated with distinct changes of surface pressure, 850 hPa winds and rainfall anomalies (Figs. 2a–d).

For higher DNS, JJAS westerlies of ISM are enhanced from the Arabian Sea to the South China Sea (SCS) and can be explained by a stronger surface pressure gradient between the southwestern IO and Asian continent (Fig. 2a). Meanwhile, JJAS rainfall is increased over most regions of India, BOB, Indo-China Peninsula, and SCS, but is decreased over Bangladesh and the TIO (Fig. 2b). However, for higher ISMR, JJAS surface pressure anomalies are dominated by negative values over the WIO in contrast to those positive values over the Indo-China Peninsula and SCS (Fig. 2c), which induce larger magnitudes of anomalous easterlies from SCS to BOB (turning to south wind anomalies over India), and only left moderate magnitudes of anomalous westerlies over the southwestern Arabian Sea. Associated rainfall is decreased in the Indo-China Peninsula and SCS, but increased in the SWIO, equatorial Indonesia, and the South Asian region (5°N – 30°N , 60°E – 95°E) (Fig. 2d).

These results suggest that, although the stronger ISM westerlies due to land–sea pressure gradients can indeed result in higher ISMR at multi-decadal scales, the interannually increased ISM rainfall should be more related to anomalous easterlies due to surface high pressure and anticyclonic circulation from SCS to BOB. The latter linkage can be explained in the context of ENSO and IOD.

3.b. Interannual modulation of ENSO on ISMR relies on IOD

Consistent with previous studies (Annamalai *et al.* 2007; Wu *et al.* 2012; Chakraborty, 2018), the SOI_{JJA} and SOI_{DJF} time series share much similarity (Fig. 1b) and their correlation with ISMR show clear seasonal inverse feature (Fig. 1f). Before the spring of Year (Yr) 1, both SOI_{JJA} (Yr 0) and SOI_{DJF} (Yr 1) are weakly related to the increased ISMR in Yr 1 ($R = -0.23$ and -0.14 , $p = 0.01$ and 0.11), but after spring, SOI_{JJA} (Yr 1) and SOI_{DJF} (Yr 2) are significantly correlated to ISMR in Yr 1 ($R = +0.42$ and $+0.50$, $p = 3.13 \times 10^{-7}$ and 5.54×10^{-10}).

Regression coefficients against the minimum of SOI_{JJA} (Yr 0, El Niño) and the maximum of SOI_{JJA} (Yr 1, La Niña) (Fig. 2e–f and Fig. 2g–h) are both featured by increased ISMR during the summer of Yr 1, accompanying with anomalous surface high pressure, anticyclonic circulation from SCS to BOB. These SOI_{JJA} associated anomalies are similar to those higher ISMR-associated changes (in Fig. 2c–d), and stand for two types of ENSO impact on ISMR (Wu *et al.* 2012; Chowdary *et al.* 2014, 2016; Chakraborty, 2018). One type is the lagged impact of decayed El Niño (from Yr0 JJA to Yr1 DJF) through the IPOC mechanism, the other is the simultaneous impact of developing La Niña through atmospheric circulation during the summer of Yr 1.

We noted that these two ENSO impacts show distinct responses in TIO that may be related to different phases of IOD. Since the SOI_{JJA} and DMI time series have a significant correlation of -0.55 ($p = 2.09 \times 10^{-12}$), it means that a summer El Niño always appear with positive IOD event (or La Niña with negative IOD). This explains those differences in zonal surface pressure gradient in TIO: The west low-east high pressure pattern (Fig. 2e) reflects the persistent effect of positive IOD during the decayed El Niño phase, and the reversed gradient (Fig. 2g) may be influenced by negative IOD during the developing La Niña phase. How will these different phases of IOD impact on ISMR?

3.c. Positive IOD can greatly suppress ISMR in the same summer

Also consistent with previous studies (Saji *et al.* 1999; Gadgil *et al.* 2004; Ihara *et al.* 2007), the correlation is $+0.07$ ($\text{lag} = 1$, $p = 0.43$) when ISMR lags DMI by 1 year (Fig. 1f), suggesting a poor lagged linkage from the DMI of Yr 0 to the ISMR of Yr 1. But this correlation becomes -0.29 ($p = 0.0006$) for $\text{lag} = 0$, indicating that ISMR will be significantly damped by positive IOD in the simultaneous summer. Similar to Li *et al.* (2017), our regression coefficients against the maximum of DMI (Yr 0) are featured by anomalous surface westerlies from BOB to SCS, and reduced rainfall in most parts of India (Fig. 3d and 3g). This negative DMI–ISMR coherence in regression and correlation analysis seems to contradict with modern AGCM simulations, in which higher ISMR will be forced by positive IOD-like SST anomalies (Ashok *et al.* 2004, 2007). But recently it has been explained by the dominant influence of ENSO on ISMR overwhelming that of IOD (Li *et al.* 2016; Hrudya *et al.* 2021). For example, during those time intervals of strong ENSO–IOD coherence, the ENSO–ISMR correlation is high, and the IOD–ISMR correlation is low (Ashok *et al.* 2001). So the decreased ISMR by El Niño may have much larger magnitude than the increased ISMR by positive IOD.

Our moving correlation shows that strong ENSO–IOD coherence mainly appears in two intervals of Yr 1883–1928 and of Yr 1969–1998 (red line in Fig. 1e). But these multidecadal (30–50 years) evolutions of ENSO–IOD coherence impact little on those of DMI–ISMR and SOI_{JJA} –ISMR coherences, which only exhibit interdecadal (20 years) fluctuations. From Yr 1871–2010 AD, the negative correlation of DMI–ISMR ($\text{lag} = 0$) becomes stronger (close to or lower than -0.4) during those time intervals of larger SOI_{JJA} –ISMR coherences ($\text{lag} = 0$) (brown and orange lines in Fig. 1d). It means that the ENSO–IOD coherence changes are hardly to explain the simultaneous negative relationship between ISMR and DMI.

Our modern sensitivity experiments of CAM4 suggest that, if forced by positive IOD-like SST anomalies during JAS, there will be only slightly increased summer rainfall over the northeastern BOB (Fig. 4b). More drastically is the decreased rainfall with anomalous surface high pressure and easterlies extending from the southwestern BOB to the Arabian Sea (Figs. 4a–4b). This anomalous meridional rainfall seesaw pattern is mainly contributed by the warmer WIO (Figs. 4c–4d), but only moderately cancelled by the cooler EIO (Figs. 4e–4f). Totally, ISMR is reduced by -0.15 mm/day over land, in which the warmer WIO and cooler EIO contribute to -0.27 mm/day and $+0.12$ mm/day, respectively.

Compared to previous studies that mainly emphasize the role of EIO cooling (Ashok *et al.* 2001, 2004; Krishnan *et al.* 2006, 2011), our CAM4 simulations illustrate the importance of WIO warming and provide another reasonable explanation for the damped ISMR

by positive IOD in the simultaneous summer. Of course, the relative contributions of WIO and EIO to ISMR may be varied temporally and depend on particular IOD-like thermal gradient or the phase combination of IOD and ENSO, or the recent global warming background. For example, our summer WIO warming induces anomalous anticlockwise circulation over WIO of 10° S– 20° N (Figs. 4a and 4c), which may weaken the climatological cross-equatorial low level jet stream and associated moisture transport into ISM regions. But this positive IOD induced feature mainly appears during those intervals of stronger ENSO–IOD coherence, and disappears in recent several decades with weaker ENSO–IOD coherence under global warming (Li *et al.* 2016; Hrudya *et al.* 2021; Chakraborty and Singhai, 2021).

3.d. Decayed IOD can also modulate upper OHC and ISMR

Moreover, the winter WIO warming during the decayed positive IOD or El Niño may also impact ISMR. Although the correlation between ISMR and JFM WIO OHC26 index ($\text{OHC26}_{\text{WIO}}$) from Yr 1871 to 2010 AD is only $+0.25$ (lag = 0, $p = 0.0029$), it is comparable to the simultaneous impact of DMI on ISMR ($R = -0.29$). For the JFM $\text{OHC26}_{\text{WIO}}$ index, the largest correlation is 0.43 ($p = 1.84 \times 10^{-7}$) with DMI (+) of Yr 0, and is -0.42 ($p = 2.17 \times 10^{-7}$) with the SOI_{DJF} of Yr 1 (Fig. 1f). Moving correlation further shows that, except for the time interval of Yr 1944–1968, its moving correlation with DMI (+) of Yr 0 is generally positive and comparable with its correlation with SOI_{DJF} of Yr 1 (black and gray lines in Fig. 1e). And at multidecadal scales, both the DMI and SOI_{DJF} show stronger coherence with $\text{OHC26}_{\text{WIO}}$ during time intervals of strong ENSO–IOD coherence and vice versa. This probably indicates a significant role of WIO OHC on ISMR that depends on the interplay of ENSO and IOD.

But the $\text{OHC26}_{\text{WIO}}$ only exhibits higher correlation (larger than $+0.4$) with ISMR during the interval of Yr 1944–1968 (cyan line and shaded in Fig. 1e), corresponding to a weakened ENSO–IOD coherence (red line in Fig. 1e). This interval is also accompanied with a sharply reduced correlation (from positive mean value of $+0.5$ to negative mean value of -0.13) between $\text{OHC26}_{\text{WIO}}$ and DMI (+) of Yr 0 (black line in Fig. 1e). Although not significant, the correlation between DMI (+) of Yr 0 and ISMR also falls from positive to negative (brown line in Fig. 1e). This may suggest for a dominant role of IOD on the winter WIO OHC and associated ISMR, because there seems to be no similar sharp changes in the coherence between SOI_{DJF} and $\text{OHC26}_{\text{WIO}}$ (gray line in Fig. 1e).

Note that the simultaneous relation between DMI (or SOI_{JJA}) and ISMR is still significant during this time interval (brown and orange lines in Fig. 1d), one possibility is that the concurrences of La Niña and negative IOD (both favoring increased ISMR) are relatively rare, as indicated by weakened SOI_{JJA} –DMI coherence. More extremely, the damping effect of positive IOD on ISMR may largely cancel the increased ISMR during the summer of La Niña. In other words, the simultaneous effects of ENSO and IOD on ISMR will be greatly reduced during time interval of weakened SOI_{JJA} –DMI coherence. This may result in a relative larger contribution of winter WIO OHC on ISMR and explain the significant coherence between them during Yr 1944–1968. But considering that most correlations among DMI, SOI, OHC, and ISMR during this interval are not significant, it is hard to resolve their true causal relationships. Here, we can only focus on the overall role of winter WIO OHC in bridging IOD and ISMR across the 20th century.

By regressing OHC26 onto the normalized timeseries of DMI (Figs. 3a–3b), we can see that positive IOD is accompanied by a zonal seesaw pattern of JAS OHC26 anomalies in the TIO, and those positive OHC26 anomalies in the WIO are still significant during JFM of next year. Interestingly, the higher ISMR-associated JFM OHC26 anomalies (Fig. 3c), JJAS surface pressure, 850hPa wind, and rainfall (Figs. 2c and 2d), all share many similarities with those of IOD-induced lagged air–sea anomalies (Figs. 3b, 3e and 3h). Note that similar features can also be found in those summer anomalies regressed onto $\text{OHC26}_{\text{WIO}}$ (Figs. 3f and 3i), it, is reasonable to say that at interannual scales of the 20th century, historical positive IOD events can also greatly modulate the upper OHC in the TIO, and result in the increased $\text{OHC26}_{\text{WIO}}$ during JFM of next year, then associated IPOC effect triggers anomalous high pressure and AAC over the SCS and BOB (Xie *et al.* 2016; Du *et al.* 2022), finally induce following JJAS ISM anomalies (surface easterlies and higher ISMR).

Using another modern sensitivity experiment of CAM4 (experiment $\text{CAM}_{\text{control_WIOsst_jfmP}}$), we can preliminarily illustrate the summer atmospheric response to the JFM SST warming anomalies in WIO. The rainfall increased over BOB and India south of 20° N but decreased over land regions north of 20° N (Fig. 4h), resulting a slightly reduced ISMR by -0.01 mm/day over land. Associated surface pressure and wind anomalies (Fig. 4g) also have smaller magnitudes and opposite signs relative to those summer SST induced changes (Figs. 4a and 4c). One reason is that the winter SST forcing ($+0.1\text{K}$ to $+0.2\text{K}$ in Figs. 4h) is smaller than the summer SST forcing of positive IOD ($+0.4\text{K}$ to $+0.6\text{K}$ in Figs. 4b). Another reason may be that those air–sea feedbacks following the winter WIO warming is also essential for the IPOC mechanism induced by positive IOD.

So far, we still cannot separate the delayed impacts of ENSO, IOD, and winter WIO warming on increased ISMR by regression analysis and CAM4 simulations. Although many studies highlighted the lagged impact of decayed El Niño on ISMR through IPOC (Mishra *et al.* 2012; Darshana *et al.* 2020), here, we argue that when the coherence of El Niño and positive IOD (in Yr 0) is higher, the decayed IOD can also result in higher JFM WIO OHC in Yr 1, and may favor the following increased ISMR. In future studies, this IOD-induced lagged impact on ISMR should be not only further separated from the simultaneous impact of IOD, but also from those simultaneous and lagged anomalies induced by ENSO.

3.e. Precession forced paleo-IOD also dominates OHC and ISMR

Previous studies have shown that precessional insolation changes can induce significant tropical air–sea coupled responses assembling modern IOD mode (Abram *et al.* 2007, 2020; Brown *et al.* 2009; Kwiatkowski *et al.* 2015; Wang *et al.* 2015; Mohtadi *et al.* 2017; Iwakiri & Watanabe, 2019; Windler *et al.* 2023). Associated zonal or meridional temperature/pressure gradients across the Indian Ocean may have greatly modulated hydroclimate changes in the African–Asian–Australian monsoon regions (Tierney *et al.* 2012; Bolton *et al.* 2013; deBoer *et al.* 2014; Weldeab *et al.* 2022). But the role of upper OHC in bridging IOD and ISMR at orbital scales is still unclear.

Figure 5 illustrates those air–sea coupled paleoclimate changes associated with higher ISMR (mainly at the precession band) from experiment CESM_ghg . During JFM, negative OHC26 anomalies dominate large areas of the Indian Ocean (especially the northeastern and southwestern parts), largely as a result of

decreased boreal winter insolation (Fig. 5a) (Wang *et al.* 2015). While during JAS, OHC26 anomalies in Figure 5b are featured by a positive IOD-like zonal seesaw pattern (similar to modern observation, Fig. 3a), mainly induced by increased boreal summer insolation (Wang *et al.* 2015). Annual mean OHC26 anomalies are generally dominated by those JAS OHC26 anomalies but also greatly reflect the contribution of JFM OHC26 anomalies (especially in the Indian Ocean south of 10° S) (Fig. 5c). The latter is also supported by the concurrence of precession parameter minima and the Mg/Ca-SST minimum of core WIND28K, reflecting decreased JFM insolation and mixed layer temperature (Fig. 6a).

In short, increased ISM rainfall at the precession band mainly corresponds to higher OHC26 in the equatorial WIO during boreal summer–autumn and also corresponds to lower OHC26 in the equatorial EIO during the whole year. Thus, the positive linkage between JFM OHC26_{WIO} and JJAS ISMR from modern interannual climate changes cannot be directly analoged to long-term paleoclimate changes, especially at the precession band with seasonal reversed insolation anomalies. It also means that the modern observed 1-year lagged response of ISMR to IOD through the bridging effect of JFM OHC26_{WIO} may be interrupted by external forcing (winter precessional insolation).

As shown in Figure 5e, higher ISMR is also accompanied by increased JJAS rainfall from the tropical Indian Ocean to equatorial Indonesia, but with reduced rainfall over the southeastern Indian Ocean, southern parts of the SCS and BOB. Note that these TIO rainfall anomalies between 15° S and 15° N are similar to modern IOD-related JJAS rainfall changes in CAM4 (Fig. 4b). Dose it means that the JJAS ISMR under precessional forcing may be also reduced by IOD-associated summer OHC anomalies in the tropical Indian Ocean?

Modern observation and simulation (Krishnan *et al.* 2006, 2011) suggest that due to intensified equatorial easterlies (during positive IOD), decreased upper OHC prevails with shallower mixed layer and local atmospheric subsidences in the equatorial EIO from June to August, which further induces remote upward motions over India through meridional vertical atmospheric circulation anomalies, and induce increased ISMR through stronger cross-equatorial monsoon flow and moisture export from the southeast Indian Ocean (Behera *et al.* 1999; Ashok *et al.* 2004). Paleoclimate proxies and simulation also show that upper ocean thermal structure changes in the EIO (and associated zonal/meridional thermal gradients) during boreal summer–autumn can significantly modulate ISM, generally with cooler EIO corresponding to stronger ISM westerlies or increased monsoon rainfall (Bolton *et al.* 2013; Weldeab *et al.* 2022). This represents a direct atmospheric linkage from the EIO to ISM during boreal summer.

Considering that the ice sheet was fixed as modern values and the ice-albedo feedback was muted in our transient simulation, the modeled glacial–interglacial climatic changes may be underestimated and hinder the direct comparison with proxy data. In Figures 6a–6c, we choose to remove the long-term trend (dashed lines) from SST proxies using 3-order polynomial fitting method and ignore those proxy-model discrepancies in magnitudes of short term changes. After detrending, those U^K_{37} -SST residuals in WIO and EIO (orange lines) show many similarities with our simulated SST (black lines) and only just lack some precessional cycles (Figs. 6b–6c). Consistent with our simulated DMI, U^K_{37} -SST based DMI is also dominated by precessional cycles except for the time interval of 120–200 ka (Fig. 6d). Moreover, these precessional cycles of two DMI indexes seem to be more contributed by EIO

changes that are out of phase with ISMR (Figs. 6c–6e). Thus, it seems that our transient simulations and paleo-proxies all support the notion of EIO-dominated IOD modulation on ISMR at the precession band.

3.f. Relative role of IOD, ENSO, and land–sea thermal contrast on ISMR at the precession band

Our simulated paleo-IOD also prevails with anomalous equatorial easterlies from the central Pacific Ocean to the WIO (Figs. 5e–5f), indicating that the climatological summer Walker circulation is enhanced over the western to central Pacific but weakened over TIO (Wang *et al.* 2015, 2019; Wang *et al.* 2018). This is in contrast to the modern observed positive IOD and El Niño combination and reflects the independent TIO response under external forcing. To explain the coupling between the two anomalous zonal-vertical circulations, we identified a meridional wave-like pattern of those rainfall anomalies (negative-positive-negative-positive) from the southeast TIO to ISM region (Fig. 5e). This meridional pattern represents three local anomalous meridional vertical atmospheric circulations (with descent-ascent-descent-ascent from south to north) (Fig. 5d), probably excited by the colder SST and atmospheric subsidence in the EIO, or by the summer oceanic warming and atmospheric upward motions in the WIO.

Although we highlight the modulation of IOD on ISMR, the precession-forced La Niña-like conditions in the western-central Pacific Ocean may also contribute to the higher ISMR. More importantly, orbital changes of ISMR (Figs. 5e and 6e) have been largely attributed to land–sea thermal difference at the precession band (Wang *et al.* 2016). Here, we further assess the relative contribution of land–sea contrast, ENSO and IOD on ISMR based on sensitivity experiments of CAM4. As a start, the influence of land–sea thermal gradient under precessional forcing can be illustrated by those JJAS differences between experiments CAM_P_{min} and CAM_{control} (Figs. 7a–7b), which are featured by anomalous surface high pressure and AAC over the North Indian Ocean, and by reduced rainfall in regions of 5° S–20° S and of 5° N–20° N, but with increased rainfall in regions of 5° S–5° N and north of 20° N. Then composite differences between experiments CAM_P_{min}_{nptpsst} and CAM_P_{min} show that the Pacific SST anomalies can induce anomalous surface low pressure and westerlies over South Asia and increased rainfall over India, BOB, and SCS regions (Figs. 7c–7d). It means that the precessional forced summer “central Pacific type” La Niña-like pattern (Wang *et al.* 2019) can produce stronger ISM westerlies and higher ISMR.

As shown by composite differences between experiments CAM_P_{min}_{TIOsst} and CAM_P_{min}, TIO SST anomalies during all seasons induce anomalous surface high pressure and more drastically reduced rainfall in the northern Arabian Sea and India (15° N–25° N), and in BOB and SCS regions (10° N–25° N) (Figs. 7e–7f). Meanwhile, significant anomalous low pressure and increased rainfall occupy the WIO and the EIO of 0° N–10° N. Additional CAM4 experiments (CAM_P_{min}_{TIOsst}_{JJA}, CAM_P_{min}_{TIOsst}_{JJAP}, and CAM_P_{min}_{TIOsst}_{JJAN}) prove that, the meridional wave-like pattern of summer rainfall from the southeast TIO to ISM region is mainly contributed by summer WIO SST anomalies (as shown by Figs. 8b and 8d). And they are accompanied by anomalous surface easterlies extending from the southwestern BOB to the Arabian peninsula, and by anomalous cross-equatorial northerlies over WIO of 10° S–20° N (Figs. 8a and 8c). Although these precessional forced anomalies are similar to those induced by modern positive IOD (Figs. 4a–4b), the EIO

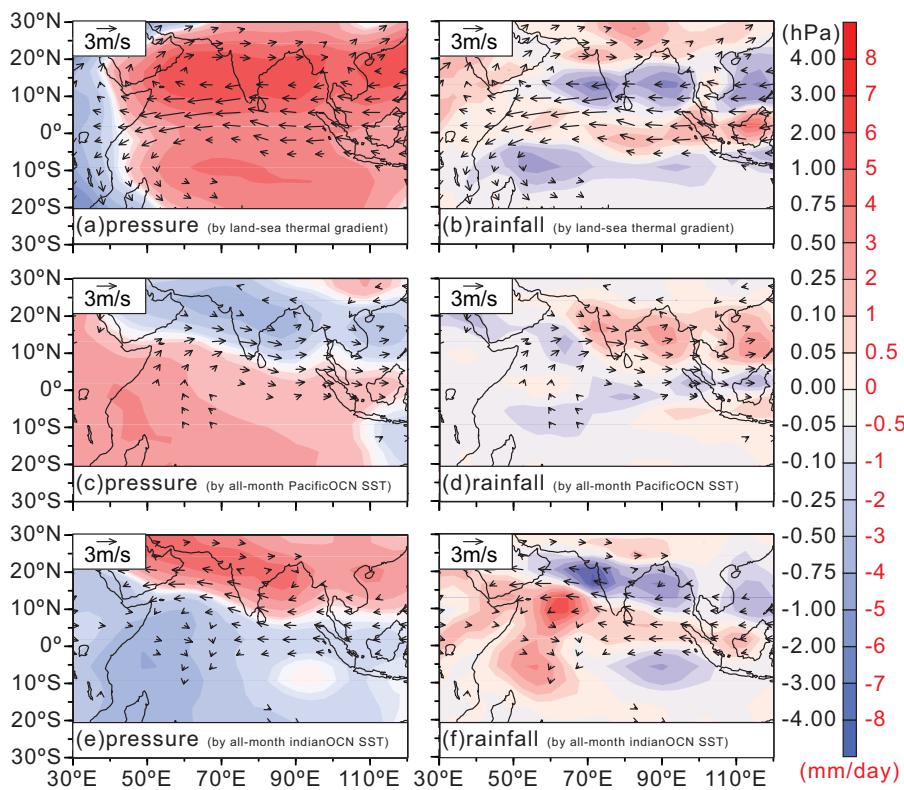


Figure 7. (Colour online) Composite differences of JJAS atmospheric variables between experiments CAM_P_{min} and CAM_{control} (a–b), between experiments CAM_P_{min_nptpsst} and CAM_P_{min} (c–d), and between experiments CAM_P_{min_TIOsst} and CAM_P_{min} (e–f). The left panels are surface pressure (shaded) and 850 hPa horizontal winds (vectors, small winds (magnitude < 0.5 m/s) are not shown). The right panels are the same as the left panels but with surface pressure replaced by rainfall (shaded). Characters in parentheses show the forcing factor for composite differences in each panel.

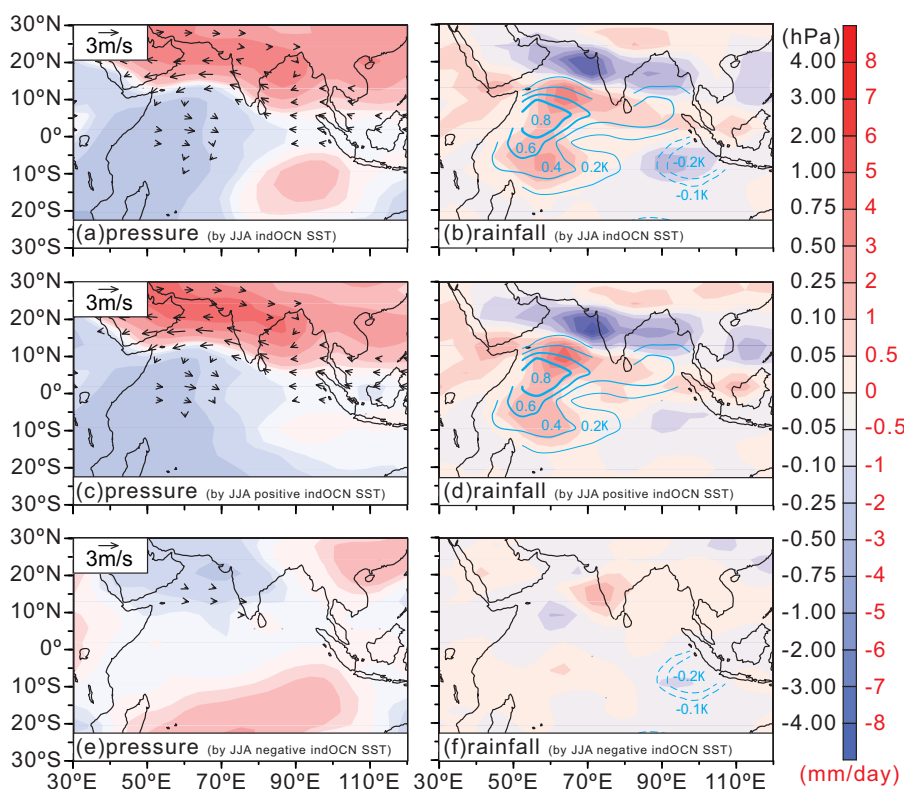


Figure 8. (Colour online) Similar to Figure 7, but for composite differences between experiments CAM_P_{min_TIOsst_JJA} and CAM_P_{min} (a–b), between experiments CAM_P_{min_TIOsst_JJAP} and CAM_P_{min} (c–d), and between experiments CAM_P_{min_TIOsst_JJAN} and CAM_P_{min} (e–f). Cyan contours in (b), (d), (f), and (h) show the spatial distributions of SST anomalies prescribed in each experiment.

wave-like rainfall pattern seems have larger meridional extension (Fig. 8b relative to Fig. 4b). This may indicate larger contributions from those SST warming anomalies in WIO and the EIO of 0° N–10° N, but can also be attributed to the smaller magnitudes of

SST cooling in the southeast TIO (–0.1 K––0.2 K, cyan contours in Fig. 8b) relative to modern situations (–0.2 K––0.6 K in Fig. 4b).

Note that the Pacific SST tends to increase the ISM rainfall everywhere, but the effect of TIO SST and land–sea contrast are

spatially inhomogeneous over the Indian subcontinent (wetter north and drier south). Totally, the ISMR is increased by +0.69 mm/day for the land–sea contrast effect and by +0.52 mm/day for the Pacific SST, but is decreased by −0.48 mm/day for the TIO SST effect. For this damping effect of TIO SST, the summer IOD-like SST anomalies only contribute −0.16 mm/day because of the mutually offsetting by WIO warming (−0.44 mm/day) and EIO cooling (+0.28 mm/day). Thus, large parts (−0.32 mm/day) of the TIO damping effect actually should be attributed to SST anomalies of autumn, winter, and spring. Moreover, if TIO SST anomalies were added to experiment CAM_P_{min_nptsst} (rather than experiment CAM_P_{min}), although associated anomalous rainfall pattern is similar, the TIO damping effect will become −0.79 mm/day and the ISMR will be only increased by +0.42 mm/day relative to experiment CAM_{control}. It means there exist significant nonlinear interactions in atmosphere when combined SST forcing from different regions.

Finally, in our equilibrium CESM simulations (experiments CESM_P_{min} and CESM_{control}), the ISMR is increased by +1.58 mm/day, close to the difference of +1.71 mm/day between 10ka and 0ka in the experiment CESM_{ghg} (Fig. 6e). This includes not only those positive contributions from land–sea contrast and paleo-ENSO (+1.2mm/day), but also the damping effect of TIO SST in different seasons (−0.48 or −0.79 mm/day, including but not limited to paleo-IOD). Clearly, there is a large gap in the magnitude of ISMR changes between CESM and CAM4. In other words, the real contribution of positive paleo-IOD to higher ISMR requires further studies by considering the role of air–sea feedbacks.

4. Conclusion and final remarks

In this study, we comprise modern observation, paleoclimate simulation and proxy reconstruction, trying to investigate the modulation of IOD and associated TIO OHC on the Indian summer monsoon rainfall from interannual to orbital time scales.

Based on historical observations from the year 1871 to 2010 AD, we illustrated that those air–sea coupled dynamics associated with ISM rainfall are entirely different from those of ISM wind at interannual time scales. While stronger ISM wind (westerlies) can indeed result in higher ISMR at the expense of a drier TIO, higher ISMR is generally associated with surface high pressure, easterly wind and reduced rainfall anomalies from SCS to BOB. These higher ISMR-associated anomalies can be firstly attributed to two types of ENSO influence, (1) the simultaneous atmospheric circulation changes of developing La Niña in Yr 1 and (2) the lagged air–sea coupled IPOC effect of decayed El Niño since Yr 0, probably bridged by the increased WIO OHC above 26°C during boreal winter–spring.

We argue that this higher ISMR-associated winter OHC anomaly can also be attributed to positive IOD conditions one year before, and this linkage is enhanced with a stronger ENSO-IOD coherence at multidecadal time scales. But the positive correlation between ISMR and winter WIO OHC is insignificant during those time intervals of stronger ENSO-IOD coherence (Yr 1883–1928 and 1969–1998). Our sensitivity experiments of CAM4 further prove that, the winter WIO SST warming anomalies only induce slightly increased ISM rainfall south of 20° N and decreased rainfall north of 20° N, while those summer positive IOD-like SST anomalies result in drastically decreased rainfall from the southwestern BOB to the northern Arabian Sea. Totally, the ISMR is changed by +0.01 and −0.15mm/day due to these two

kinds of SST anomalies. It means that the impact of winter WIO OHC on ISMR through IPOC mechanism is only secondary, probably overwhelmed by the simultaneous impacts of El Niño and positive IOD.

By comparing paleoclimate simulation and paleo-proxies, we found that modern interannual positive linkage between ISMR and winter WIO OHC was cut off by seasonal reversed insolation anomalies at the precessional band. But our CAM4 experiments also prove the precessional forced ISMR can be simultaneously damped by positive IOD-like OHC anomalies in the summer TIO. Similar to modern situations, we identified a meridional wave-like pattern of summer rainfall anomalies from the southeast TIO to ISM region, and the drastically decreased rainfall in the southern ISM region dominates the total ISMR changes. This damping effect is mainly contributed by the warmer western TIO that triggers anomalous easterlies along the southern flank of surface high pressure anomalies from BOB to Arabian Peninsula. And the cooler southeastern TIO will only moderately increase rainfall in the southern ISM region.

Finally, our transient simulation results are generally consistent with paleo-temperature proxies from the tropical Indian Ocean, and the simulated $\delta^{18}\text{O}_{\text{sw_GISS}}$ in the Bay of Bengal from experiment GISS_{ghg} are also similar to ISMR and negative $\delta^{18}\text{O}$ peaks are nearly in phase with high ISM rainfall (Figs. 6e–6f), confirming the dominant role of ISMR on the freshwater supplement to the Bay of Bengal (Clemens *et al.* 2021; Tabor *et al.* 2018). Our simulated $\delta^{18}\text{O}_{\text{sw_GISS}}$ shows large discrepancies relative to the proxy-reconstructed $\delta^{18}\text{O}_{\text{sw_ivc}}$ (Fig. 6f), probably due to the coarse resolution and model limitation of our GISS_{ModelE2-R} model, or due to the errors of temperature correction and seasonal biases of $\delta^{18}\text{O}_{\text{sw_ivc}}$ proxy, which all require for more future studies.

Acknowledgements. This work was supported by the National Natural Science Foundation of China (Y.W., grant number 41976047), (X.W., grant number 42106060), (S.Z., grant number 42376053), (H.D., grant number 42176053, 42222603), and (Z.J., grant numbers 42188102, 91958208). Y.W. is also sponsored by the National Key Research and Development Program of China (grant number: 2023YFF0803904) and by the Shanghai Pilot Program for Basic Research. Y.W. acknowledges the Shanghai Supercomputer Center and the Beijing Super Cloud Computing Center (BSCC) for providing HPC resources that have contributed to the research results reported within this paper.

Competing interests. The authors declare none.

References

- Abram NJ, Gagan MK, Liu ZY, Hantoro WS, McCulloch MT and Suwargadi BW (2007) Seasonal characteristics of the Indian Ocean Dipole during the Holocene epoch. *Nature* **445**, 299–302.
- Abram NJ, Hargreaves JA, Wright NM, Thirumalai K, Ummenhofer CC and England MH (2020) Palaeoclimate perspectives on the Indian Ocean Dipole. *Quaternary Science Reviews* **237**, 106302.
- Ali MM, Nagamani PV, Sharma N, Gopal RTV, Rajeevan M, Goni GJ and Bourassa MA (2015) Relationship between ocean mean temperatures and Indian summer monsoon rainfall. *Atmospheric Science Letters* **16**, 408–413.
- Annalai H, Hamilton K and Sperber KR (2007) The South Asian summer monsoon and its relationship with ENSO in the IPCC AR4 simulations. *Journal of Climate* **20**, 1071–1092.
- Aschok K, Saji NH (2007) On the impacts of ENSO and Indian Ocean dipole events on sub-regional Indian summer monsoon rainfall. *Natural Hazards* **42**, 273–285.

- Ashok K, Guan Z, Yamagata T (2001) Impact of the Indian Ocean dipole on the relationship between the Indian monsoon rainfall and ENSO. *Geophysical Research Letters* **28**, 4499–4502.
- Ashok K, Guan Z, Saji NH and Yamagata T (2004) Individual and combined influences of ENSO and the Indian Ocean dipole on the Indian summer monsoon. *Journal of Climate* **17**, 3141–3154.
- Ashok K, Behera SK, Rao SA, Weng H and Yamagata T (2007) El Niño Modoki and its possible teleconnection. *Journal of Geophysical Research* **112**, C11007.
- Bard E, Rostek F and Sonzogni C (1997) Interhemispheric synchrony of the last deglaciation inferred from alkenone palaeothermometry. *Nature* **385**, 707–710.
- Behera SK, Krishnan R, Yamagata T (1999) Unusual oceanatmosphere conditions in the tropical Indian ocean during 1994. *Geophysical Research Letters* **26**, 3001–3004.
- Biasutti M, Voigt A, Boos WR, Braconnot P, Hargreaves JC, Harrison SP, Kang S, Mapes, BE, Scheff J, Schumacher C, Sobel AH and Xie S (2018) Global energetics and local physics as drivers of past, present and future monsoons. *Nature Geoscience* **11**, 392–400.
- Bolton CT, Chang L, Clemens SC, Kodama K, Ikehara M, Medina-Elizalde M, Paterson GA, Roberts AP, Rohling EJ, Yamamoto Y and Zhao X (2013) A 500,000 year record of Indian summer monsoon dynamics recorded by eastern equatorial Indian Ocean upper water-column structure. *Quaternary Science Reviews* **77**, 167–180.
- Brown J, Lynch AH and Marshall AG (2009) Variability of the Indian Ocean Dipole in coupled model paleoclimate simulations. *Journal of Geophysical Research* **114**, D11105.
- Budziak D, Schneider RR, Rostek F, Müller PJ, Bard E and Wefer G (2000) Late Quaternary insolation forcing on total organic carbon and C37 alkenone variations in the Arabian Sea. *Paleoceanography* **15**, 307–321.
- Carton JA, Seidel HF and Giese BS (2012) Detecting historical ocean climate variability. *Journal of Geophysical Research* **117**, C02023.
- Chakraborty A (2018) Preceding winter La Niña reduces Indian summer monsoon rainfall. *Environmental Research Letters* **13**, 054030.
- Chakraborty A and Singhai P (2021) Asymmetric response of the Indian summer monsoon to positive and negative phases of major tropical climate patterns. *Scientific Reports* **11**, 22561.
- Chen ZS, Li ZN, Du Y, Wen ZP, Wu RG and Xie SP (2021) Trans-Basin Influence of Southwest Tropical Indian Ocean Warming during Early Boreal Summer. *Journal of Climate* **34**, 9679–9691.
- Cheng LJ, Trenberth KE, Fasullo J, Boyer T, Abraham J and Zhu J (2017) Improved estimates of ocean heat content from 1960 to 2015. *Science Advances* **3**, e1601545.
- Cheng LJ, von Schuckmann K, Abraham JP, Trenberth KE, Mann ME, Zanna L, England MH, Zika JD, Fasullo JT, Yu Y, Pan Y, Zhu J, Newsom ER, Bronselaer B and Lin X (2022) Past and future ocean warming. *Nature Reviews Earth & Environment* **3**, 776–794.
- Chowdary JS, Chaudhari HS, Gnanaseelan C, Parekh A, Rao AS, Sreenivas P, Pokhrel S and Singh P (2014) Summer monsoon circulation and precipitation over the tropical Indian Ocean during ENSO in the NCEP climate forecast system. *Climate Dynamics* **42**, 1925–1947.
- Chowdary JS, Parekh A, Kakatkar R, Gnanaseelan C, Srinivas G, Singh P and Roxy MK (2016) Tropical Indian Ocean response to the decay phase of El Niño in a coupled model and associated changes in south and east-Asian summer monsoon circulation and rainfall. *Climate Dynamics* **47**, 831–844.
- Clemens SC, Yamamoto M, Thirumalai K, Giosan L, Richey JN, Nilsson-Kerr K, Rosenthal Y, Anand P and McGrath SM (2021) Remote and local drivers of Pleistocene South Asian summer monsoon precipitation: a test for future predictions. *Science Advances* **7**, eabg3848.
- Darshana P, Chowdary JS, Gnanaseelan C, Parekh A and Srinivas G (2020) Interdecadal modulation of the Indo-western Pacific Ocean Capacitor mode and its influence on Indian summer monsoon rainfall. *Climate Dynamics* **54**, 1761–1777.
- de Boer EJ, Tjallingii R, Vélez M, Rijsdijk K, Vlug A, Reichert GJ, Prendergast AL, de Louw PGB, Vincent Florens FB, Baider C and Hooghiemstra H (2014) Climate variability in the SW Indian Ocean from an 8000-yr long multi-proxy record in the Mauritian lowlands shows a middle to late Holocene shift from negative IOD-state to ENSO-state. *Quaternary Science Reviews* **86**, 175–189.
- De Vleeschouwer D (2010) Time-series analysis on selected geological sections: A search for cyclicity. Thesis for degree of Master, Faculty of Science and Bio-engineering Sciences, Department of Geography, Vrije University Brussel. p105.
- Du Y, Xie SP, Huang G and Hu K (2009) Role of air-sea interaction in the long persistence of El Niño-induced North Indian Ocean warming. *Journal of Climate* **22**, 2023–2038.
- Du Y, Yang L and Xie SP (2011) Tropical Indian Ocean influence on Northwest Pacific tropical cyclones in summer following strong El Niño. *Journal of Climate* **24**, 315–322.
- Du Y, Chen Z, Xie SP, Zhang LY, Zhang Y and Cai Y (2022) Drivers and characteristics of the Indo-western Pacific Ocean capacitor. *Frontiers in Climate* **4**, 1014138.
- Du Y, Wang F, Wang T, Liu W, Liang L, Zhang Y, Chen Y, Liu J, Wu W, Yu K and Zhang J (2023) Multi-scale ocean dynamical processes in the Indo-Pacific Convergence Zone and their climatic and ecological effects. *Earth-Science Reviews* **237**, 104313.
- Fasullo J and Webster PJ (2002) Hydrological signatures relating the Asian summer monsoon and ENSO. *Journal of Climate* **15**, 3082–3095.
- Fasullo JT and Trenberth KE (2008) The annual cycle of the energy budget. Part I: global mean and land-ocean exchanges. *Journal of Climate* **21**, 2297–2312.
- Gadgil S (2003) The Indian monsoon and its variability. *Annual Review of Earth and Planetary Sciences* **31**, 429–467.
- Gadgil S (2014) El Niño and the summer monsoon of 2014. *Current Science* **106**, 1335–1336.
- Gadgil S (2018) The monsoon system: land-sea breeze or the ITCZ? *Journal of Earth System Science* **127**, 1–29.
- Gadgil S and Srinivasan J (2011) Seasonal prediction of the Indian monsoon. *Current Science* **100**, 343–353.
- Gadgil S, Rajeevan M and Francis PA (2007) Monsoon variability: links to major oscillations over the equatorial Pacific and Indian oceans. *Current Science* **93**, 182–194.
- Gadgil S, Vinayachandran PN and Francis PA (2003) Droughts of the Indian summer monsoon: role of clouds over the Indian Ocean. *Current Science* **85**, 1713–1719.
- Gadgil S, Vinayachandran PN, Francis PA and Gadgil S (2004) Extremes of Indian summer monsoon rainfall, ENSO, equatorial Indian Ocean Oscillation. *Geophysical Research Letters* **31**, L12213.
- Geen R, Bordoni S, Battisti DS and Hui K (2020) Monsoons, ITCZs, and the concept of the global monsoon. *Reviews of Geophysics* **58**, e2020RG000700.
- Hammer Ø, Harper DAT and Ryan PD (2001) PAST: Paleontological statistics software package for education and data analysis. *Palaeontologia Electronica* **4**, 9.
- Hill SA (2019) Theories for past and future monsoon rainfall changes. *Current Climate Change Reports* **5**, 160–171.
- Hrudya PPVH, Varikoden H and Vishnu RN (2021) Changes in the relationship between Indian Ocean dipole and Indian summer monsoon rainfall in early and recent multidecadal epochs during different phases of monsoon. *International Journal of Climatology* **41**, E305–E318.
- Ihara C, Kushnir Y, Cane MA and De la Peña V (2007) Indian summer monsoon rainfall and its link with ENSO and the Indian Ocean climate indices. *International Journal Of Climatology* **27**, 179–187.
- Iwakiri T and Watanabe M (2019) Strengthening of the Indian Ocean Dipole with increasing seasonal cycle in the mid-Holocene. *Geophysical Research Letters* **46**, 8320–8328.
- Jalil CA, Bosmans JHC, Srinivasan J and Chakraborty A (2019a) The response of tropical precipitation to Earth's precession: the role of energy fluxes and vertical stability. *Climate of the Past* **15**, 449–462.
- Jalil CA, Srinivasan J, & Chakraborty A (2019b) Modulation of Indian monsoon by water vapor and cloud feedback over the past 22,000 years. *Nature Communications* **10**, 5701.
- Jian ZM, Wang Y, Dang HW, Mohtadi M, Rosenthal Y, Lea DW, Liu ZF, Jin HY, Ye LM, Kuhnt W and Wang XX (2022) Warm pool ocean heat content regulates ocean-continent moisture transport. *Nature* **612**: 92–99.

- Johnstone HJH, Kiefer T, Elderfield H and Schulz M (2014) Calcite saturation, foraminiferal test mass, and Mg/Ca-based temperatures dissolution corrected using XDX—A 150 ka record from the western Indian Ocean. *Geochemistry, Geophysics, Geosystems* **15**, 781–797.
- Kiefer T, McCave IN and Elderfield H (2006) Antarctic control on tropical Indian Ocean sea surface temperature and hydrography. *Geophysical Research Letters* **33**, L24612.
- Kumar KK, Rajagopalan B and Cane MA (1999) On the weakening relationship between the Indian monsoon and ENSO. *Science* **284**, 2156–2159.
- Kumar KK, Hoerling M and Rajagopalan B (2005) Advancing dynamical predictions of the Indian monsoon rainfall. *Geophysical Research Letters* **32**, L08704.
- Kumar KK, Rajagopalan B, Hoerling MP, Bates GT and Cane MA (2006) Unraveling the Mystery of Indian Monsoon Failure During El Niño. *Science* **314**, 115–119.
- Krishnan R, Ramesh KV, Samala BK, Meyers G, Slingo JM and Fennessy MJ (2006) Indian Ocean-monsoon coupled interactions and impending monsoon droughts. *Geophysical Research Letters* **33**, L08711.
- Krishnan R, Sundaram SK, Sundaram SK, Swapna P, Kumar V, Kumar V, Ayantika DC and Mujumdar M (2011) The crucial role of ocean-atmosphere coupling on the Indian monsoon anomalous response during dipole events. *Climate Dynamics* **37**, 1–17.
- Kothawale DR and Rajeevan M (2017) Monthly, Seasonal and Annual Rainfall Time Series for All- India, Homogeneous Regions and Meteorological Subdivisions: 1871–2016, *IITM Research Report* No. RR-138, August 2017.
- Kutzbach JE, Liu XD, Liu ZY and Chen GS (2008) Simulation of the evolutionary response of global summer monsoons to orbital forcing over the past 280,000 years. *Climate Dynamics* **30**, 567–579.
- Kwiatkowski C, Prange M, Varma V, Steinke S, Hebbeln D and Mohtadi M (2015) Holocene variations of thermocline conditions in the eastern tropical Indian Ocean. *Quaternary Science Reviews* **114**, 33–42.
- Laskar J, Robutel P, Joutel F, Gastineau M, Correia AC, Correia AC and Levrard B (2004) A long-term numerical solution for the insolation quantities of the Earth. *Astronomy and Astrophysics* **428**, 261–285.
- Lauterbach S, Andersen N, Wang YV, Blanz T, Larsen T and Schneider RR (2020) An ~130 kyr record of surface water temperature and $\delta^{18}\text{O}$ from the northern bay of bengal: investigating the linkage between heinrich events and weak monsoon intervals in Asia. *Paleoceanography and Paleoclimatology* **35**, e2019PA003646.
- Lewis SC, LeGrande AN, Schmidt GA and Kelley M (2014) Comparison of forced ENSO-like hydrological expressions in simulations of the preindustrial and mid-Holocene. *Journal of Geophysical Research: Atmospheres* **119**, 7064–7082.
- Li JP and Zeng QC (2002) A unified monsoon index. *Geophysical Research Letters* **29**, 1274.
- Li ZG, Cai WJ and Lin XP (2016) Dynamics of changing impacts of tropical Indo-Pacific variability on Indian and Australian rainfall. *Scientific Reports* **6**, 31767.
- Li ZG, Lin XP and Cai WJ (2017) Realism of modelled Indian summer monsoon correlation with the tropical Indo-Pacific affects projected monsoon changes. *Scientific Reports* **7**, 4929.
- Lückge A, Mohtadi M, Rühlemann C, Scheeder G, Vink A, Reinhardt L and Wiedicke M (2009) Monsoon versus ocean circulation controls on paleoenvironmental conditions off southern Sumatra during the past 300,000 years. *Paleoceanography*, **24**, PA1208.
- Lutsko NJ, Marshall J and Green B (2019) Modulation of monsoon circulations by cross-equatorial ocean heat transport. *Journal of Climate* **32**, 3471–3485.
- McPhaden MJ and Nagura M (2013) Indian Ocean dipole interpreted in terms of recharge oscillator theory. *Climate Dynamics* **42**, 1569–1586.
- Mishra, V, Smoliak BV, Lettenmaier DP and Wallace JM (2012) A prominent pattern of year-to-year variability in Indian summer monsoon rainfall. *Proceedings of the National Academy of Sciences of the United States of America* **109**, 7213–7217.
- Mohtadi M, Lückge A, Steinke S, Groeneveld J, Hebbeln D and Westphal N (2010a) Late Pleistocene surface and thermocline conditions of the eastern tropical Indian Ocean. *Quaternary Science Reviews* **29**, 887–896.
- Mohtadi M, Steinke S, Lückge A, Groeneveld J and Hathorne EC (2010b) Glacial to Holocene surface hydrography of the tropical eastern Indian Ocean. *Earth and Planetary Science Letters* **292**, 89–97.
- Mohtadi M, Prange M, Schefuß E and Jennerjahn TC (2017) Late Holocene slowdown of the Indian Ocean walker circulation. *Nature Communications* **8**, 1015.
- Pottapinjara V, Girishkumar MS, Sivareddy S, Ravichandran M and Murtugudde R (2016) Relation between the upper ocean heat content in the equatorial Atlantic during boreal spring and the Indian monsoon rainfall during June–September. *International Journal of Climatology* **36**, 2469–2480.
- Pu SZ, Yu F, Hu XM and Chen XR (2003) Spatial and temporal variability of heat content above the thermocline in the tropical Pacific Ocean. *Acta Oceanologica Sinica* **22**, 179–190.
- Rajeevan M and McPhaden M J (2004) Tropical Pacific upper ocean heat content variations and Indian summer monsoon rainfall. *Geophysical Research Letters* **31**, L18203.
- Rajeevan M and Pai DS (2007) On the El Niño-Indian monsoon predictive relationships. *Geophysical Research Letters* **34**, L04704.
- Ropelewski CF and Jones PD (1987) An extension of the Tahiti-Darwin Southern Oscillation Index. *Monthly Weather Review* **115**, 2161–2165.
- Rostek F, Bard E, Beaufort L, Sonzogni C and Ganssen GM (1997) Sea surface temperature and productivity records for the past 240 kyr in the Arabian Sea. *Deep-sea Research Part II* **44**, 1461–1480.
- Russell GL, Miller JR and Rind D (1995) A coupled atmosphere-ocean model for transient climate change. *Atmosphere-Ocean* **33**, 683–730.
- Russell GL, Miller JR, Rind DH, Ruedy RA, Schmidt GA and Sheth S (2000) Comparison of model and observed regional temperature changes during the past 40 years. *Journal of Geophysical Research* **105**, 14891–14898.
- Saher MH, Jung SJA, Elderfield H, Greaves MJ and Kroon D (2007) Sea surface temperatures of the western Arabian Sea during the last deglaciation. *Paleoceanography* **22**, PA2208.
- Saher MH, Rostek F, Jung SJA, Bard E, Schneider RR, Greaves MJ, Ganssen GM, Elderfield H and Kroon D (2009) Western Arabian Sea SST during the penultimate interglacial: a comparison of UK'37 and Mg/Ca paleothermometry. *Paleoceanography* **24**, PA2212.
- Saji NH, Goswami BN, Vinayachandran PN and Yamagata T (1999) A dipole mode in the tropical Indian Ocean. *Nature* **401**, 360–363.
- Schmidt GA, Hoffmann G, Shindell DT and Hu Y (2005) Modeling atmospheric stable water isotopes and the potential for constraining cloud processes and stratosphere-troposphere water exchange. *Journal of Geophysical Research: Atmospheres* **110**, 021314.
- Schmidt GA, Kelley M, Nazarenko LS, Ruedy R, Russell GL, Aleinov I, Bauer M, Bauer SE, Bhat MK, Bleck R, Canuto V, Chen Y, Cheng Y, Clune TL, Del Genio AD, de Fainchtein R, Faluvegi GS, Hansen JE, Healy RJ, Kiang NY, Koch DM, Lacis AA, Legrande AN, Lerner J, Lo KK, Matthews E, Menon S, Miller RL, Oinas V, Olosio AO, Perlwitz JP, Puma MJ, Putman WM, Rind D, Romanou A, Sato M, Shindell DT, Sun S, Syed RA, Tausnev N, Tsigaridis K, Unger N, Voulgarakis A, Yao M and Zhang J (2014) Configuration and assessment of the GISS ModelE2 contributions to the CMIP5 archive. *Journal of Advances in Modeling Earth Systems* **6**, 141–184.
- Shields CA, Bailey DA, Danabasoglu G, Jochum M, Kiehl JT, Levis S and Park S (2012) The low-resolution CCSM4. *Journal of Climate* **25**, 3993–4014.
- Slivinski LC, Compo GP, Whitaker JS, Sardeshmukh PD, Giese BS, McColl C, Allan R, Yin X, Vose R, Titchner HA, Kennedy JJ, Spencer L, Ashcroft L, Brönnimann S, Brunet M, Camuffo D, Cornes RC, Cram TA, Crouthamel RI, Dominguez-Castro F, Freeman JE, Gergis J, Hawkins E, Jones PD, Jourdain S, Kaplan A, Kubota H, Blancq FL, Lee T, Lorrey AM, Luterbacher J, Maugeri M, Mock CJ, Moore GW, Przybylak R, Pudmenzky C, Reason CJ, Slonosky VC, Smith CA, Tinz B, Trewin B, Valente MA, Wang X, Wilkinson C, Wood KR and Wyszynski P (2019) Towards a more reliable historical reanalysis: improvements for version 3 of the twentieth century reanalysis system. *Quarterly Journal of the Royal Meteorological Society* **145**, 2876–2908.
- Slivinski LC, Compo GP, Sardeshmukh PD, Whitaker JS, McColl C, Allan R, Brohan P, Yin X, Smith CA, Spencer L, Vose R, Rohrer M, Conroy RP, Schuster D, Kennedy JJ, Ashcroft L, Brönnimann S, Brunet M, Camuffo D, Cornes RC, Cram TA, Dominguez-Castro F, Freeman JE,

- Gergis J, Hawkins E, Jones P, Kubota H, Lee TC, Lorrey AM, Luterbacher J, Mock CJ, Przybylak R, Pudmenzky C, Slonosky VC, Tinz B, Trewin B, Wang XL, Wilkinson C, Wood KR and Wyszyński P (2021) An evaluation of the performance of the twentieth century reanalysis version 3. *Journal of Climate* **34**, 1417–1438.
- Tabor C.R, Otto-Bliesner BL, Brady EC, Nusbaumer JM, Zhu J, Erb MP, Wong TE, Li Z and Noone DC (2018) Interpreting precession-driven $\delta^{18}\text{O}$ variability in the South Asian monsoon region. *Journal of Geophysical Research: Atmospheres* **123**, 5927–5946.
- Tierney JE, Oppo DW, LeGrande AN, Huang Y, Rosenthal Y and Linsley BK (2012) The influence of Indian Ocean atmospheric circulation on Warm Pool hydroclimate during the Holocene epoch. *Journal of Geophysical Research* **117**, D19108.
- Trenberth KE, Stepaniak DP and Caron JM (2000) The global monsoon as seen through the divergent atmospheric circulation. *Journal of Climate* **13**, 3969–3993.
- Trenberth KE and Fasullo JT (2013) Regional energy and water cycles: transports from ocean to land. *Journal of Climate* **26**, 7837–7851.
- Venugopal T, Ali MM, Bourassa MA, Zheng Y, Goni G, Foltz GR and Rajeevan M (2018) Statistical Evidence for the Role of Southwestern Indian Ocean Heat Content in the Indian Summer Monsoon Rainfall. *Scientific Reports* **8**, 12092.
- Wang B, Liu J, Kim HJ, Webster PJ, Yim SY and Xiang B (2013) Northern hemisphere summer monsoon intensified by mega-El Niño-southern oscillation and Atlantic multidecadal oscillation. *Proceedings of the National Academy of Sciences* **110**, 5347–5352.
- Wang PX, Clemens S, Beaufort L, Braconnot P, Ganssen G, Jian ZM and Sarnthein M (2005) Evolution and variability of the Asian monsoon system: state of the art and outstanding issues. *Quaternary Science Reviews* **24**, 595–629.
- Wang PX, Wang B, Cheng H, Fasullo J, Guo Z, Kiefer T and Liu Z (2014) The global monsoon across time scales: coherent variability of regional monsoons. *Climate of the Past* **10**, 1–46.
- Wang PX, Wang B, Cheng H, Fasullo JT, Guo Z, Kiefer T and Liu Z (2017) The global monsoon across time scales: mechanisms and outstanding issues. *Earth-Science Reviews* **174**, 84–121.
- Wang Y, Jian ZM, Zhao P, Chen JM and Xiao D (2015) Precessional forced evolution of the Indian Ocean Dipole. *Journal of Geophysical Research-Oceans* **120**, 3747–3760.
- Wang Y, Jian ZM, Zhao P, Xiao D and Chen JM (2016) Relative roles of land-and ocean-atmosphere interactions in Asian-Pacific thermal contrast variability at the precessional band. *Scientific Reports* **6**, 28349.
- Wang Y, Jian ZM, Zhao P, Xu K, Dang HW, Liu ZF, Xiao D, Chen JM (2019) Precessional forced zonal triple-pole anomalies in the tropical Pacific annual cycle. *Journal of Climate* **32**, 7369–7402.
- Wang XX, Jian ZM, Lückge A, Wang Y, Dang HW, Mohtadi M (2018) Precession-paced thermocline water temperature changes in response to upwelling conditions off southern Sumatra over the past 300,000 years. *Quaternary Science Reviews* **192**, 123–134.
- Webster PJ and Yang S (1992) Monsoon and ENSO: selectively interactive systems. *Quarterly Journal of the Royal Meteorological Society* **118**, 877–926.
- Webster PJ, Magana VO, Palmer TN, Shukla J, Tomas RA, Yanai MU and Yasunari T (1998) Monsoons: processes, predictability, and the prospects for prediction. *Journal of Geophysical Research-Oceans* **103**, 14451–14510.
- Weldeab S, Rühlemann C, Ding QH, Khon V, Schneider B and Graya WR (2022) Impact of Indian Ocean surface temperature gradient reversals on the Indian Summer Monsoon. *Earth and Planetary Science Letters* **578**, 117327.
- Windler G, Tierney JE and deMenocal PB (2023) Hydroclimate variability in the equatorial western Indian Ocean for the last 250,000 years. *Paleoceanography and Paleoclimatology* **38**, e2022PA004530.
- Windler G, Tierney JE, DiNezio PN, Gibson K and Thunell RC (2019) Shelf exposure influence on Indo-Pacific warm pool climate for the last 450,000 years. *Earth and Planetary Science Letters* **516**, 66–76.
- Wu GX, Liu YM, He B, Bao Q, Duan AM and Jin FF (2012) Thermal controls on the Asian summer monsoon. *Scientific Reports* **2**, 404.
- Wu RG, Chen JL and Chen W (2012) Different types of ENSO influences on the Indian summer monsoon variability. *Journal of Climate* **25**, 903–920.
- Xie SP, Annamalai H, Schott FA and McCreary JP (2002) Structure and mechanisms of South Indian Ocean climate variability. *Journal of Climate* **15**, 864–878.
- Xie SP, Hu KM, Hafner J, Tokinaga H, Du Y, Huang G and Sampe T (2009) Indian Ocean capacitor effect on Indo-western Pacific climate during the summer following El Niño. *Journal of Climate* **22**, 730–747.
- Xie SP, Kosaka Y, Du Y, Hu K, Chowdary JS and Huang G (2016) Indo-western Pacific Ocean capacitor and coherent climate anomalies in post-ENSO summer: a review. *Advances in Atmospheric Sciences* **33**, 411–432.
- Yang XX, Wu XF, Liu ZH and Yuan CX (2019) A preliminary study on an upper ocean heat and salt content of the western Pacific warm pool region. *Acta Oceanologica Sinica* **38**, 60–71.
- Yang YP, Xiang R, Zhang L, Zhong F and Zhang M (2019) Is the upward release of intermediate ocean heat content a possible engine for low-latitude processes? *Geology* **48**, 579–583.
- Yang YP, Zhang L L, Yi L, Zhong FC, Lu ZY, Wan S, Du Y and Xiang R (2023) A contracting intertropical convergence zone during the early Heinrich stadial 1. *Nature Communications* **14**, 4695.
- Zhang L, Han WQ, Karanaskas KB, Meehl GA, Hu AX, Rosenbloom N and Shinoda T (2019) Indian Ocean warming trend reduces Pacific warming response to anthropogenic greenhouse gases: an interbasin thermostat mechanism. *Geophysical Research Letters* **46**, 10882–10890.